



# This is to certify that the

#### thesis entitled

CONVENTIONAL AND HIGH-RESOLUTION TRANSMISSION ELECTRON MICROSCOPY STUDY OF SPIN-GLASS/AMORPHOUS-SILICON MULTILAYERS

## presented by

David A. Howell

Department of Materials Science and Mechanics

has been accepted towards fulfillment of the requirements for

\_\_\_\_\_\_degree in <u>Engineering</u>

Major professor

Date\_\_\_11/10/95

**O**-7639

MSU is an Affirmative Action/Equal Opportunity Institution

# LIBRARY Michigan State University

PLACE IN RETURN BOX to remove this checkout from your record. TO AVOID FINES return on or before date due.

	The state of the s				
	DATE DUE	DATE DUE	DATE DUE		
, a	99 02 FT8				
	00° 700 58'				

MSU is An Affirmative Action/Equal Opportunity Institution

# CONVENTIONAL AND HIGH-RESOLUTION TRANSMISSION ELECTRON MICROSCOPY STUDY OF SPIN-GLASS/AMORPHOUS-SILICON MULTILAYERS

Ву

David A. Howell

## **A THESIS**

Submitted to
Michigan State University
in partial fulfillment of the requirements
for the degree of

**MASTER OF SCIENCE** 

Department of Materials Science and Mechanics

### **ABSTRACT**

# CONVENTIONAL AND HIGH-RESOLUTION TRANSMISSION ELECTRON MICROSCOPY STUDY OF SPIN-GLASS/AMORPHOUS-SILICON MULTILAYERS

By

#### David A. Howell

Conventional and high-resolution transmission electron microscopy have been used to investigate the structure and growth behavior of three separate multilayer systems composed of spin-glass alloys (Au<sub>.97</sub>Fe<sub>.03</sub>, Cu<sub>.85</sub>Mn<sub>.15</sub>, and Ag<sub>.91</sub>Mn<sub>.09</sub>) alternating with amorphous-silicon. Each of the three systems was fabricated with two different sample configurations. The first consisted of bilayers with 3 nm spin-glass alloy and 7 nm amorphous-silicon layers. The second consisted of 7 nm spin-glass alloy and 7 nm amorphous-silicon layers. CTEM and HRTEM images of cross-sectioned samples revealed variations in the degree of crystallinity of the spin-glass material. Variations in the amount and symmetry of interlayer formation were also observed. Systematic studies of such variations should help to explain differences in their measured spin-glass properties.

## **ACKNOWLEDGMENTS**

This research was supported by a grant to the Center for Fundamental Materials Research from the State of Michigan Research Excellence Fund. I would like to thank Drs. M.A. Crimp, J. Bass, J.A. Cowen, P.A. Schroeder, W.P. Pratt Jr., L. Hoines, and J. Heckman for their guidance and advice. I would also like to thank Dr. J.F. Mansfield of the Electron Microbeam Analytical Laboratory (EMAL) at the University of Michigan for his technical assistance.

# TABLE OF CONTENTS

LIST OF TABLES	vi
LIST OF FIGURES	vii
CHAPTER 1 INTRODUCTION	1
1.1 Thin-Film Multilayers	1
1.2 Metallic Spin-Glass Multilayers	3
1.3 Previous Electron Microscopy Investigations of Thin-Film Multilayers	5
1.4 Molybdenum / Amorphous-Silicon Multilayers	7
1.5 Titanium/Amorphous-Silicon Multilayers	23
1.6 Tungsten/Amorphous-Silicon Multilayers	25
1.7 Nickel/Amorphous-Silicon Multilayers	27
1.8 Relevance of Previous Work to Present Study	28
CHAPTER 2 EXPERIMENTAL PROCEDURES AND MATERIALS	30
2.1 Spin-Glass Multilayer Fabrication	30
2.2 CTEM Specimen Preparation using Ultramicrotomy	33
2.3 HRTEM Specimen Preparation	36
CHAPTER 3 EXPERIMENTAL RESULTS	52
3.1 CTEM of Microtomed Multilayers	52
3.2 HRTEM of Ion-Milled Multilayers	62

3.3 TEM and X-ray Characterization of Bilayer Periodicity	9
CHAPTER 4 DISCUSSION	3
4.1 Experimental Factors Which Complicate Image Interpretation	3
4.2 Crystallinity and Interlayer Mixing in Multilayers	4
4.3 Effect of Interface Structure on Spin-Glass Properties	8
CHAPTER 5 CONCLUSIONS8	1
LIST OF REFERENCES	2

# LIST OF TABLES

Table 1.1	CTEM and HRTEM studies of metal/amorphous-silicon multilayers 9
Table 1.2	Molybdenum/amorphous-Si multilayer parameters [39] 11
Table 1.3	Deposition and fabrication parameters of multilayers [54]
Table 1.4	Calculated average incident energy at substrate [54]
Table 1.5	Mo/a-Si multilayers fabricated with heated substrate [58]
Table 1.6	Surface energy density as function of substrate bias [62]
Table 1.7	Surface energy density as function of Ar <sup>+</sup> pressure [62]
Table 1.8	Tungsten/amorphous-Si multilayer parameters [79]
Table 2.1	Sputtering parameters of spin-glass layers [18]
Table 3.1	Bilayer periodicity in spin-glass multilayers
Table 4.1	Comparison of degree of spin-glass crystallinity from different methods 76

# LIST OF FIGURES

Figure	1.1	Idealized multilayer structure.	. 2
Figure	1.2	Transition temperature vs. CuMn layer thickness. After Kenning [8]	. 4
Figure	1.3	Reduced temperature vs. CuMn layer thickness. After Kenning [8]	. 6
Figure	1.4	Multilayer features characterized by TEM	. 8
Figure	2.1	Multilayer sample configurations	32
Figure	2.2	Large angle x-ray scans of <111> peaks in spin-glass multilayers.  After Hoines [18]	34
Figure	2.3	Multilayer removal from silicon substrate.	35
Figure	2.4	Sequence for ultramicrotomy sectioning and collecting ultrathin sections.	37
Figure	2.5	Low magnification CTEM of ultrathin sections on grid	38
Figure	2.6	Higher magnification CTEM of multilayer embedded in epoxy resin	39
Figure	2.7	Composite slab, slotted-rod, tube, and molybdenum rings.	40
Figure	2.8	Sectioned discs of slotted-rod and tube specimen	42
Figure	2.9	Sectioned disc on Pyrex <sup>™</sup> stub	43
Figure	2.10	Sectioned disc and stub in Gatan™ Disc Grinder	44
Figure	2.11	Dimpler wheel and TEM specimen on Pyrex™ stub	45
Figure	2.12	SEM image of TEM specimen after dimpling and ion-milling	47
Figure	2.13	Fabrication of slab-on-ring type specimen.	48
Figure	2.14	a) Slotted-rod and tube b) slab-on-ring specimen configurations	50

Figure	2.15	SEM image of differential milling at multilayer/substrate interface	51
Figure	3.1	CTEM of Au <sub>.97</sub> Fe <sub>.03</sub> /Si 3 nm/7 nm multilayer	53
Figure	3.2	CTEM of Au <sub>.97</sub> Fe <sub>.03</sub> /Si 7 nm/7 nm multilayer	54
Figure	3.3	a) Bright-field b) Dark-field CTEM images of altered Au <sub>.97</sub> Fe <sub>.03</sub> /Si 3 nm/ 7 nm multilayer	56
Figure	3.4	CTEM of Cu <sub>.85</sub> Mn <sub>.15</sub> /Si 3 nm/7 nm multilayer.	57
Figure	3.5	CTEM of Cu <sub>.85</sub> Mn <sub>.15</sub> /Si 7 nm/7 nm multilayer.	58
Figure	3.6	CTEM of Ag <sub>.91</sub> Mn <sub>.09</sub> /Si 3 nm/7 nm multilayer	60
Figure	3.7	CTEM of Ag <sub>.91</sub> Mn <sub>.09</sub> /Si 7 nm/7 nm multilayer	61
Figure	3.8	a) Low magnification and b) enlarged area of Cu <sub>.85</sub> Mn <sub>.15</sub> /Si 7 nm/7 nm multilayer.	63
Figure	3.9	a) Low magnification and b) enlarged area of Cu <sub>.85</sub> Mn <sub>.15</sub> /Si 3 nm/7 nm multilayer.	64
Figure	3.10	a) Low magnification and b) enlarged area of Au <sub>.97</sub> Fe <sub>.03</sub> /Si 7 nm/ 7 nm multilayer.	66
Figure	3.11	a) Low magnification and b) enlarged area of Au <sub>.97</sub> Fe <sub>.03</sub> /Si 3 nm/ 7 nm multilayer.	67
Figure	3.12	a) Low magnification and b) enlarged area of Ag <sub>.91</sub> Mn <sub>.09</sub> /Si 3 nm/7 nm multilayer.	68
Figure	3.13	Small-angle x-ray scan of Au <sub>.97</sub> Fe <sub>.03</sub> /Si 7 nm/7 nm multilayer. After Hoines [18]	70
Figure	4.1	Finite-size effects of CuMn, AgMn, and AuFe spin-glasses with silicon into layers. After Hoines [18].	
Figure	4.2	Finite-size effects of CuMn, AgMn, and AuFe spin-glasses with silicon into layers and corrected spin-glass thicknesses. After Hoines [18]	

#### CHAPTER 1 INTRODUCTION

### 1.1 Thin-Film Multilayers

With the advent of ultra-high vacuum sputtering systems it has become possible to create artificial superlattices containing a vast range of elements [1]. By depositing alternating layers of two different elements a multilayer structure can be created (Figure 1.1). With the ability to fabricate these multilayers many physical phenomena which arise from the unique geometries or juxtaposition of compositional layers can be investigated. Examples of such investigations include the focusing of soft x-rays with multilayers of alternating high and low atomic number materials [2, 3], giant magnetoresistance in multilayers of magnetic and non-magnetic elements [4, 5], and superconductivity of artificially layered materials [6, 7]. One other field in which multilayers have been used extensively is in the study of spin-glass alloys [8-18].

The multilayers fabricated to investigate the properties of spin-glass alloys typically consist of tens of alternating layers of a spin-glass metal alloy and a non-metallic layer to isolate the spin-glass. Because the structure and composition are critical to the determination of finite size effects in spin-glass material the focus of this study is three-fold. One, to determine if the layering in the multilayers is continuous and uniform. Two, to characterize the crystallinity within each layer, if any exists. Three, to investigate the presence of interfacial mixing at the interface of the alternating layers. The approach used

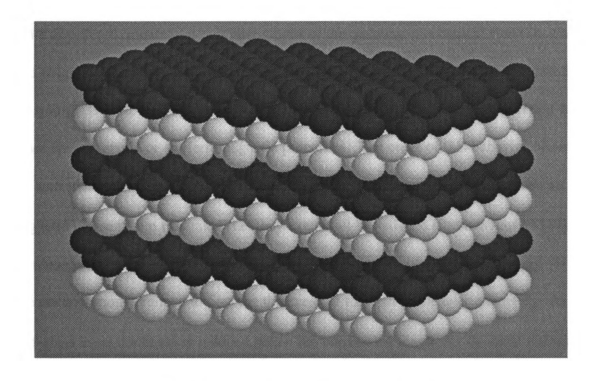


Figure 1.1 Idealized multilayer structure.

to accomplish the above tasks is a combination of conventional transmission electron microscopy (CTEM) and high-resolution transmission electron microscopy (HRTEM).

## 1.2 Metallic Spin-Glass Multilayers

A metallic spin-glass is a metal alloy which consists of a bulk elemental metal doped with a dilute amount of an elemental magnetic species. The term spin-glass refers to the disordered orientations and interactions of the quantum-mechanical spin (i.e. a nonzero magnetic moment) possessed by the magnetic species [17]. This disorder provides the spin-glass with the interesting trait of displaying cooperative behavior different from either ferromagnetic or antiferromagnetic properties. The onset of this behavior occurs at the spin-glass ordering temperature, T<sub>g</sub>, where the alignment interactions between the magnetic moments are frustrated (i.e. they cannot all be satisfied simultaneously) [19]. A phenomenon of interest to current spin-glass studies is that of finite-size scaling [8-11]. The phenomenon is related to how the thickness of the spin-glass layer affects T<sub>g</sub>. As the spin-glass layer thickness is reduced below the correlation length for the bulk material a downward shift in T<sub>g</sub> occurs (Figure 1.2) [8]. Finite-size scaling refers to the changes in physical properties when one dimension of a three-dimensional system is restricted to a length, L. In this case, the theory predicts that the fractional temperature change in  $\boldsymbol{T}_g,\,\boldsymbol{\epsilon},$ will scale as:

$$\varepsilon = T_g^b - T_g / T_g^b \approx L^{-\gamma}$$

where  $T^b_{\ g}$  is the bulk value of the spin-glass ordering temperature and  $\gamma$  is the scaling

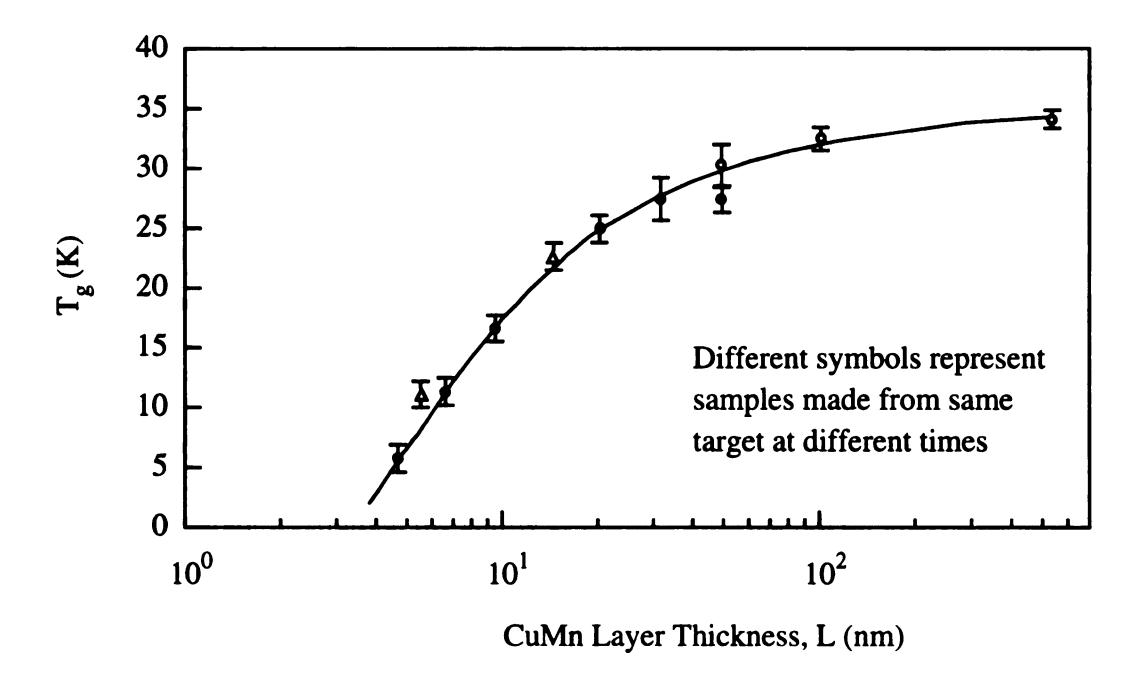


Figure 1.2 Transition temperature vs. CuMn layer thickness. After Kenning [8].

exponent. Strictly, this equation only applies vigorously when  $\varepsilon$  is small. Figure 1.3 is a plot of  $\varepsilon$  vs. L [8].

# 1.3 Previous Electron Microscopy Investigations of Thin-Film Multilayers

Since this study is concerned with metallic spin-glass/amorphous-silicon multilayers, a review of only metal/amorphous-silicon systems is necessary. A majority of these studies have been on multilayers fabricated as potential soft x-ray optical elements [20]. An additional field of study incorporating metal/amorphous-silicon multilayers arises from the concern of the semiconductor industry about the thermodynamic stability of these systems, which are models of metal-semiconductor contact interfaces [21-24]. Many of the early studies into the structure of multilayers utilized the technique of x-ray diffraction to determine bilayer period and the uniformity of layers. Although this technique has the advantage of being non-destructive and relatively quick with little or no sample preparation required, the ability to provide information on interfacial structure and chemistry is complicated by the need for extensive computer modelling of the diffraction profile [25-28]. In the past decade, innovations in cross-sectional sample preparation techniques for multilayers have allowed the investigation of the structure of multilayers using transmission electron microscopy. The non-equilibrium deposition conditions which exist during the fabrication of multilayers have led to systematic studies of the conditions which affect the final multilayer structure [29]. The resultant structure and chemical stability of the multilayer is subject to both kinetic and thermodynamic factors [30, 31]. The influence of sputtering pressure, substrate, temperature, and the heat of mixing between the component layers have all been shown to affect the multilayer structure [32].

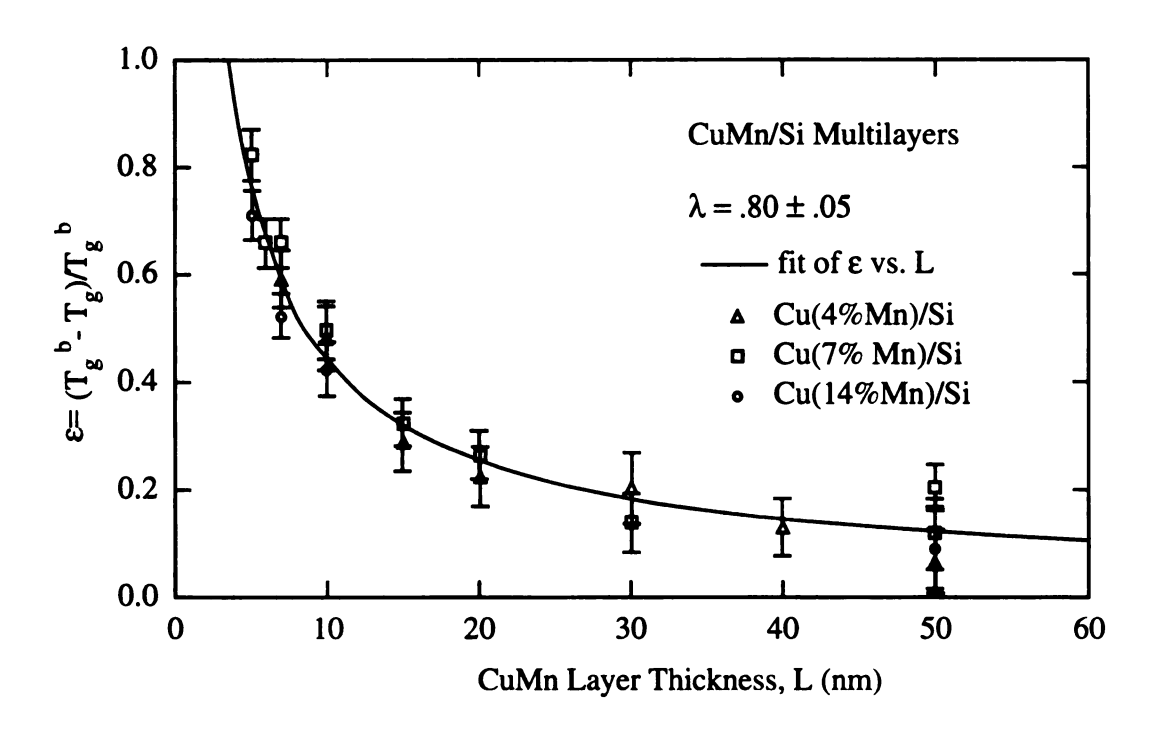


Figure 1.3 Reduced temperature vs. CuMn layer thickness. After Kenning [8].

One interesting discovery resulting from the study of multilayers has been the characterization of the solid-state amorphization reaction (SSAR) which only occurs for specific combinations of compositional, thermodynamic, and kinetic influences [33-35]. In contrast to the technique of X-ray diffraction, which samples the whole multilayer structure, the use of cross-sectional transmission electron microscopy provides information on a relatively small portion of the specimen. The use of TEM in the study of multilayers has provided direct evidence for the propagation of coherent layer roughness and the existence of interfacial reactions between layers. It is this detailed localized information that makes electron microscopy a useful complimentary technique to x-ray diffraction. Various features of the multilayers which can be investigated by the use of CTEM and HRTEM are illustrated in Figure 1.4.

In addition to CTEM and HRTEM studies, various alternative electron microscopy techniques such as Z-contrast (a.k.a. High-angle annular dark-field), STEM [36, 97, 100], Fresnel method [82], and electron holography [64], have been utilized to provide chemical spatial resolution. Several metal/amorphous-silicon systems have received a considerable amount of attention, most notably Mo/Si, Ti/Si, W/Si, and Ni/Si. A list of the systems studied to date is provided in Table 1.1. To aid in the interpretation of the experimental results from this investigation a review of the pertinent aspects of several previous CTEM and HRTEM studies of the various multilayer systems is provided.

# 1.4 Molybdenum / Amorphous-Silicon Multilayers

Because of their importance as optical elements in soft X-ray ( $\Lambda$ =13nm) projection lithography, an emphasis has been placed on research into the structure and stability of

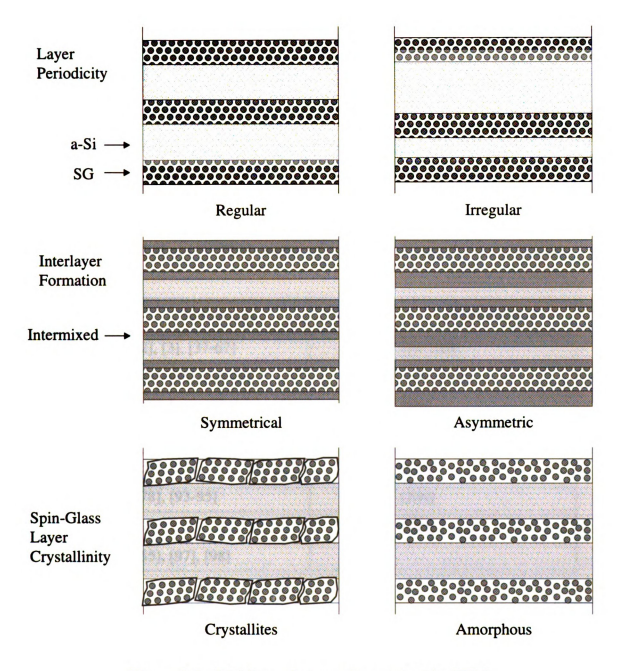


Figure 1.4 Multilayer features characterized by TEM.

Table 1.1 CTEM and HRTEM studies of metal/amorphous-silicon multilayers.

Metal	References	Metal	References
Мо	Mo [2], [3], [37-67]		[98-100]
Ti	[43], [45], [68-78]	V	[70], [101]
W	[39], [50], [79-83]	Cr	[70]
Ni	[84-90]	Pd	[102]
Co	[38], [53], [70], [91], [92]	Y	[103]
Al	[78], [93-95]	Pt	[104]
Nb	[96]	Fe	[105]
Ru	[55], [97], [98]		

multilayers composed of Mo and amorphous silicon. Several observations concerning the multilayer structure are common to all studies of this system.

One of the earliest studies on this system by Petford-Long et al. [39] examined seven different Mo/a-Si multilayer samples (Table 1.2). The as-deposited structure of the multilayers revealed by HRTEM was an amorphous Si layer followed by a 1.7(0.3) nm thick amorphous interfacial region of Mo and Si and then a crystalline Mo layer followed by another amorphous region of mixed Mo and Si which was only 1.0(0.3) nm thick. This morphology was observed in all the samples, regardless of the number of bilayers or individual layer widths. The last two samples which were fabricated with a different sputtering system also maintained the same asymmetric interfacial regions.

In an annealing study of Mo/a-Si multilayers, Holloway et al. [42], found that the as-deposited multilayer contained a similar asymmetric interfacial structure, with a Moon-Si intermixed region of 1.9 nm and a 1.1 nm thickness for the Si-on-Mo interface. The bilayer spacing from low-angle X-ray scattering was 13 nm. The composition determined from Rutherford backscattering spectrometry was 36 at% Mo, 63 at% Si, and 1 at% Ar. The authors speculated that greater momentum of Mo atoms during deposition may account for the larger Mo-on-Si region. It was also suggest that the release of latent heat of condensation may account for increased interdiffusion, driven by a negative heat of mixing.

In a study of the effect of substrate temperature and deposition rates in the electron-beam deposition of the Mo/a-Si multilayers, Sudoh et al. [46] reported the existence of interdiffusion in five of seventeen samples synthesized. These samples were made either with a higher deposition rate (1 nm/sec vs. 0.2 nm/sec) or increased substrate

Table 1.2 Molybdenum/amorphous-Si multilayer parameters [39].

Bilayer thickness (nm)	Mo-layer thickness (nm)	Si-layer thickness (nm)	Number of Bilayers	Mo-on-Si interface (nm)	Si-on-Mo interface (nm)
11.2	5.6	5.3	25	1.7	1.0
6.7	4.3	2.4	11	1.7	1.0
11.3	5.8	5.5	5	-	-
11.3	6.5	4.7	50	-	-
11.3	5.5	5.2	7	-	-
11.7	8.7	2.8	50	-	-
11.4	9.2	3.0	50	-	-

temperature (280° C and 420° C vs. 100° C). The observations were based on TEM cross-sectional micrographs, but no measurements of intermixed regions were reported and the basis for the evidence of intermixing was not explained. In all the micrographs shown it is worth noting that the amorphous silicon layers have an apparent width which is approximately 2-3 times thinner than the Mo layers even though the intended fabrication parameters were to create 3 nm Mo-layers and 4 nm Si-layers. No mention of this discrepancy was made by the authors, but it could be explained by either thick TEM sections or more interdiffusion than perceived by the authors.

A comprehensive investigation by Boher et al. [53] into the formation of the interfacial regions of Mo/a-Si multilayers employed several experimental techniques; in-situ kinetic ellipsometry (KE), low- and high angle x-ray diffractometry, Auger electron spectroscopy (AES), Rutherford backscattering spectrometry (RBS), and HRTEM. Four samples with five bilayers were fabricated with varying intended Mo-layer thicknesses (2.4, 3.9, 6.7, 10.1 nm) and constant (10 nm) Si-layers. Simulations of the RBS spectra based on the multilayer configuration and the known densities of the pure component layers (Mo and Si) were coupled with the layer widths observed in the HRTEM images to derive the density of the metal layer for the smallest Mo-layer sample (2.4 nm). Based on the simulations it was concluded the Mo-layer was mostly a Mo-Si alloy. The HRTEM images of this multilayer indicated that both the silicon and Mo-Si alloy were amorphous with no indication of crystalline Mo being present. With increasing intended Mo-layer thicknesses, crystalline Mo is detected and the coherence length is calculated from the highangle x-ray diffraction peaks of the <220> reflection using the Scherrer formula. These coherence lengths are still less than the intended thickness of the Mo-layers. For the

sample with the intended Mo-layer thickness of 6.7 nm it was reported that the Mo-on-Si interface was 1.5 nm thick and the Si-on-Mo interface was 0.8 nm thick. No interfacial widths were given for the other two samples. From modelling in-situ KE the researchers reported that during deposition of Mo on Si that approximately 1 nm of Si and 0.6 nm of Mo are involved in the formation of the interfacial region. For the case of Si being deposited onto Mo they calculate that 0.7 nm of Si and 0.5 nm of Mo are reacting to form the silicide layer. In both cases more Si is being consumed, but with increased amounts for the Mo-on-Si case. The increased thickness of the interfacial region of the Mo-on-Si interface was attributed not to the different depositional parameters of the Mo and Si from the targets but rather to the decreased surface reactivity of crystalline Mo compared to the amorphous silicon.

A study of the multilayer morphology dependence on the sputtering gas pressure was conducted by Stearns et al. [54]. Four samples were fabricated with Ar pressures ranging from 2.5 to 20 mTorr. The deposition and fabrication parameters are listed in Table 1.3. As the Ar pressure increased, the multilayers exhibited a transition from layer growth, where each successive layer is flat, to columnar growth, where each successive layer exhibits increased curvature localized about domed columns propagating from the substrate. As in the previous studies, the Mo layers are crystalline with a strong <110> texture while the Si layers are amorphous. In addition, the microstructure of the multilayer exhibited similar asymmetric interfacial regions. For the Mo-on-Si and the Si-on-Mo interfaces, the average widths were 1.0 (0.1) nm and 0.5 (0.1) nm, respectively. In this study, the authors explained the dependence of multilayer morphology on the sputtering gas in terms of the energy transferred to the growth surface by adatoms and Ar neutrals.

Table 1.3 Deposition and fabrication parameters of multilayers [54].

Ar Pressure (mTorr)	Mo Deposition rate (nm/s)	Si Deposition rate (nm/s)	Multilayer Period (nm)	Mo Crystallites (nm)
2.5	0.48	0.63	6.74	2.65
5	0.32	0.52	6.85	2.88
10	0.29	0.45	6.79	2.88
20	0.26	0.30	7.96	4.0-0.8

Based on the calculations of Somekh [106], they were able to estimate the values of the average adatom (Mo, Si) and Ar neutral energies as a function of Ar pressure (Table 1.4). It is evident that the Ar neutrals provide a significant contribution to the energy input arriving at the surface and that it is strongly dependent on the Ar pressure. The decrease in the quality of the multilayers (i.e. increased layer roughness) is explained in terms of a reduction of surface mobility of the adatoms. Since the activation energies of adatom motion are fractions of an electron-volt (0.2-0.8 eV) the increased energy of the incident Ar neutrals provides enough local heating to allow the adatoms to migrate to more energetically favorable sites. This low energy configuration manifests itself in the Mo/Si system in the form of Mo crystallites with the <110> planes oriented in the growth direction. An additional benefit of the increased surface mobility of the adatoms is that the amorphous silicon layer is able to smooth over the polycrystalline Mo layer. Although this model provides a reason for the trend in increased layer roughness with Ar pressure, it still does not explain the asymmetry of the interfacial regions since the average incident energy contribution of the Si and Mo adatoms are essentially equivalent over the Ar pressures with the exception of the highest value (Table 1.4).

In a study of the optimal growth parameters, Stearns et al. [58] compared the microstructure of Mo/Si multilayers grown by ultra high vacuum deposition (UHVD) and magnetron sputtering. The growth conditions of the two techniques differ mainly in the adatom energies (0.1 eV for UHVD and 1.0-2.0 eV for sputtering). Another key difference is the incident angle of the atoms arriving at the deposition surface. In UHVD this angle is near normal to the multilayer surface, whereas in magnetron sputtering there is large angular spread. Two parameters that were studied in this investigation were the

Table 1.4 Calculated average incident energy at substrate [54].

Ar Pressure (mTorr)	E <sub>Si</sub> (ev)	E <sub>Mo</sub> (ev)	E <sub>Ar</sub> (ev)
2.5	11	11	80
5.0	8	8	67
10	5	4	40
20	1.6	0.8	16

substrate temperature and deposition rate. In all the samples fabricated using UHVD and magnetron sputtering an amorphous region formed between the Mo and Si layers. In both sets of samples it was observed that the thickness of the Mo-on-Si interlayer was greater than the Si-on-Mo interlayer. Table 1.5 shows the samples with the temperature of deposition, the bilayer period from the small-angle x-ray scan (SAXS), the Mo-crystallite size from the large-angle x-ray scan (LAXS), and the average thickness of each of the four regions discernible in the HREM images. Stearns et al. [58] attribute this to different degrees of penetration and interdiffusion of the Si and Mo adatoms during deposition. However, their data do suggest that the thickness of the amorphous interlayer of the Mo-on-Si layer is partly dependent on the substrate temperature. Using a least squares fit to the equation:

$$t-t_0 \propto e^{-E_g/(kT)}$$

yielded an activation energy of 0.23 eV and a value of the ambient Mo-on-Si thickness,  $t_0 = 1.5$  nm. This relation is based on the supposition that the thickness,  $t_0$ , of the Mo-on-Si interfacial layer is composed of a temperature independent part,  $t_0$ , and a temperature dependent part,  $t_0$ . This activation energy value is comparable to the measured surface diffusion activation energy of other metal-substrate systems, but much less than the value of the bulk interdiffusion activation energy measured for sputtered Mo/Si systems. They postulate that interlayer growth at the Mo-on-Si interface is strongly controlled by surface diffusion but that the Si-on-Mo interlayer is not. Two other observations they cite to support their hypothesis are the constant thickness of the interface throughout the layers (i.e. the earliest layers show no increased diffusion) and that the Si-on-Mo interfaces are

Table 1.5 Mo/a-Si multilayers fabricated with heated substrate [58].

Substrate Temp. (K)	Crystallite Size of Mo (nm)	Mo-layer thickness (nm)	Si-layer thickness (nm)	Mo-on-Si interface (nm)	Si-on-Mo interface (nm)
300	5.1	5.4	4.2	1.5	0.6
400	2.2	2.7	4.2	1.6	0.5
425	2.4	2.5	3.7	1.7	0.5
475	2.4	2.2	4.4	1.8	0.7
500	2.2	1.8	4.3	1.8	0.6
525	2.2	2.2	3.9	2.0	0.5
525	2.2	2.2	3.8	2.0	0.7
550	2.2	2.1	3.6	2.3	0.5
575	2.1	2.3	3.8	2.3	0.5

relatively abrupt with respect to the change in diffraction contrast between the purely amorphous silicon and crystalline Mo.

In an effort to reduce the deposition-induced amorphization of interfaces in Mo/Si multilayers a study by Jankowski [59] concentrated on the thermalization of sputtered neutrals and the adjustment of the source-to-substrate distance. Thermalization is the process by which the kinetic energy of the sputtered material is reduced by scattering as a result of interaction with the sputter gas. The increase in gas pressure randomizes the near-normal incident path of the incoming adatoms. Jankowski noted that the sputter gas pressure must be adjusted such that the adatoms have enough surface mobility to facilitate smoothing but not enough energy as to cause interdiffusion. To promote smooth layering with sharp interfaces, Jankowski considered it crucial to work with long source-to-substrate distances and low sputter gas pressures. With a working gas pressure of 5.5 mTorr and a 10 cm source-to-substrate distance, Jankowski calculated the sputtered atom energies as 4.7 eV for Si and 3.9 eV for Mo. With these deposition parameters the Mo-on-Si interface was 0.5 nm wide and the Si-on-Mo interface showed an "atomically abrupt" transition. An alternate method of improving the structural quality of magnetron sputtered Mo/Si multilayers was reported by Vernon et al. [62]. As mentioned in the two previous studies, working at greater Ar pressures decreases the surface mobility of the adatoms which prevents the growth of smooth layers. However, at low Ar pressures, amorphous or compositionally graded interfaces can result. Vernon et al. found that applying a negative bias to the substrate produced an ion-bombardment of the growing film by the Ar sputtering gas ions. The supplemental energy provided by this technique allowed deposition of material at higher sputtering gas pressures thereby thermalizing the Ar neutrals while still giving the adatoms sufficient surface mobility to form smooth layers (Table 1.6). A set of four separate experiments in which the substrate bias was maintained at 0 v, -100 v, -200 v and -300 v revealed that a layered morphology with no propagating roughness could be obtained at deposition pressures as high as 10 mTorr as long as a negative bias was present. It was also discovered that with an increase of bias from -100 v to -300 v the amount of interdiffusion was significantly increased to the point were the pure molybdenum layer was completely consumed and a Mo-Si alloy layer remained in its place. In another set of experiments the bias voltage was applied during the deposition of only the Mo or Si layers and compared to the samples prepared with no bias and bias during deposition of both layers. From the HRTEM images it was clear that the significant improvement of the multilayer quality is associated only with a bias on the substrate during Si deposition and that a bias maintained during the Mo sputtering had a negligible effect on morphology. This behavior was explained by evaluating the surface energy densities (eV/adatom) as a function of sputtering pressure (Table 1.7). The value of the energy flux at the film surface during deposition was computed as a sum of the contributions from the reflected Ar neutrals and adatom kinetic energies normalized to their deposition rate. Although the contribution from the kinetic energies of the Si and Mo are roughly equivalent (~ 10 ev/atom) the amount of reflected Ar neutrals produced during sputtering is vastly different. The flux of reflected Ar is governed by the mass ratio of the target atoms and sputtering gas which is 0.7 for Si (28 amu) and 2.4 for Mo (96 amu) when Ar is used (40 amu). For target atoms that are less massive there is no appreciable quantity of reflected sputter gas atoms, whereas for the heavier target atoms almost 40% of the incident Ar atoms are reflected. Thus, reflected Ar neutrals contribute significantly to

Table 1.6 Surface energy density as function of substrate bias [62].

Substrate Bias (V)	Mo Surface Energy (ev/Mo atoms)	Si Surface Energy (ev/Si atoms)	
0	99	5	
-100	108	22	
-200	141	45	
-300	177	75	

Table 1.7 Surface energy density as function of Ar<sup>+</sup> pressure [62].

Deposition Pressure (mTorr)	Mo Surface Energy (ev/Mo atoms)	Si Surface Energy (ev/Si atoms)
1.75	164	12
5	154	8
10	99	5
20	56	2

the surface energy density during the sputtering of Mo and this contribution will decrease as the sputtering gas pressure is increased. However, there is still adequate surface energy for the Mo adatoms to rearrange on the growth surface in a low-energy configuration. This is not the case for Si adatoms at higher sputtering gas pressures so it is necessary to bias the substrate to produce ion bombardment of the surface during Si deposition.

## 1.5 Titanium/Amorphous-Silicon Multilayers

Because of its importance to very large-scale integration (VLSI) interconnect technology, the Ti-Si system has been the focus of several studies concerned with the stability of multilayers and interfaces of Ti and Si. An early study by Holloway and Sinclair [68] investigated the thermal stability of two multilayer compositions of 40% Si - 60% Ti and 60% Si - 40% Ti. The bilayer periodicity was 10 nm. In an unannealed Si-rich as-deposited sample the Ti-on-Si and Si-on-Ti interface each consisted of an equivalent 1.2-1.4 nm planar intermixed amorphous region.

In a study of a-Si-Ti-a-Si trilayers with respective thicknesses of 72(2), 23(1), and 72(2) nm, Raaijmakers et al. [71] found that the rf-diode sputtered samples contained an interfacial region 2.5 nm wide. They derived this estimate from Si AES depth profile which also indicated a symmetric intermixing region for the Si-on-Ti and Ti-on-Si interface. In a later study, Raaijmakers and Kim [75] found that in a-Si/Ti/x-Si trilayers the interfaces of a-Si/Ti and Ti/x-Si consisted of amorphous regions of approximately 2.4(0.3) nm in width. In their discussion they outline the possible cause of intermixing during deposition by sputtering. They explained that the symmetrical Si-on-Ti and Ti-on-Si interfacial mixing regions result from the similar mass of the Ti, Si, and Ar. As in the case of the

Mo/Si multilayers, the sputtering process creates Ar neutrals which bombard the deposition surface with particles possessing energies between 100-1000 eV. Because the cross-section for the neutralization and reflection of the lighter Ar ions bombarding a heavier target like Mo is large, one expects a larger flux of energetic particles then when a lighter target material such as silicon is used. This would explain the larger intermixing region at the Mo-on-Si interface. Thus, the smaller mass difference between Ti, Si, and Ar would account for the symmetrical interfacial mixing regions.

A HRTEM in-situ annealing study (Holloway et al. [42]) of sputtered deposited Ti/Si multilayers with a 25 nm bilayer periodicity revealed that all as-deposited interfaces between the a-Si and x-Ti had an amorphous mixed region 2.9 nm in width. In a later study Holloway et al. [45] compared silicide formation in four metal-Si systems (metal = Mo, Ni, Ti, Co) and found that in all of the as-deposited systems there were amorphous interfacial regions between the metal and silicon layers. However, only the Mo-Si multilayers showed a marked asymmetry in width of Mo-on-Si interface as compared to the Sion-Mo interface. They suggested that latent heat resulting from the condensing Mo vapor would aide the intermixing of the Mo with the deposited Si. Furthermore, they ascribe the asymmetric interfaces to the large difference between the heats of sublimation of the Mo and Si components (664.5 and 450.1 kj/g at. respectively).

Ogawa et al. [76] studied Ti thin-films sputter deposited onto a variety of surface modified Si-substrates. All of the doped single-crystal Si-substrates (p, p+, n+) had an intermixing region of 1.7(.3) nm, whereas the amorphized Si substrate had an intermixing region of 2.5(.3) nm.

# 1.6 Tungsten/Amorphous-Silicon Multilayers

Because of the large differences in atomic number of the component layers, the W-Si system has also been examined as a potential multilayer focusing element for soft x-rays. One of the first reports of a W-Si multilayer examined by HRTEM was by Petford-Long et al. [39]. The multilayer had an average bilayer thickness of 2.8(.3) nm as measured from the HRTEM images. Although a distinct layering of light and dark contrasting materials with measured thicknesses of 1.5(.4) and 1.3(.4) nm existed, there was no discernible region which was crystalline W. The intended fabrication parameters were a Si layer of 20.0 nm and a W layer of 5.0 nm resulting in a bilayer periodicity of 25.0 nm. It was observed that the interfaces of Si-on-W were sharper than the W-on-Si interfaces.

Nutt and Keem [79] conducted a HRTEM study of five magnetron-sputtered W/Si multilayer samples with various bilayer periodicities and individual layer widths. Table 1.8 lists the bilayer thickness, W and Si bilayer thickness percentages of the bilayers, and the interface thickness. No crystalline W was reported in any of the multilayer samples.

W/Si multilayers with a bilayer width of 1.5 nm (0.6 nm W and 1.0 nm Si) fabricated by Vidal and Marfaing [81] also showed no indication of crystalline W. HRTEM and selected-area electron diffraction (SAED) results indicated that the layers were amorphous and the interfaces were atomically smooth. They attribute the amorphization in the W-layer to the formation of an amorphous WSi complex.

An attempt to extract quantitative information about the intermixing at the W-Si interface was made by Shih and Stobbs [82]. By modeling the profile intensity of a through-focal series (i.e. a set of images with incremental defocus change) of Fresnel

Table 1.8 Tungsten/amorphous-Si multilayer parameters [79].

Bilayer thickness (nm)	W-thickness bilayer %	Si-thickness bilayer %	Interface thickness (nm)
9.2	40	60	0.55
5.15	39	61	0.5
1.87	60	40	not available
1.48	70	30	not available

between the W and Si layers in two multilayer samples with bilayer thicknesses of 6.5 and 2.3 nm with respective W layers thicknesses of 2.16 nm and 0.95 nm. Dark field images of the smaller period multilayer did indicate however, that portions of the layer presumed to be W were microcrystalline. Due to the small size of the crystallites it was not possible to determine whether the material was pure W or a W silicide phase.

A set of five W/Si multilayers fabricated by magnetron sputtering was studied by Dupuis et al. [80]. From TEM observations of samples microcleaved from the multilayers, it was determined that all of the multilayers except the largest period size sample were amorphous.

Brunel et al. [83] prepared six W/Si multilayer samples by electron beam deposition. It was determined by LAXS and SAED that all of the multilayers lacked any crystal-line W material despite the fact that the layers were evaporated and not sputtered.

## 1.7 Nickel/Amorphous-Silicon Multilayers

In a study of Ni-silicide formation, Holloway and Clevenger [86] investigated the annealing behavior of a 10 nm period Ni-Si multilayer with 7 nm Ni and 10 nm Si layers. SAED patterns indicate that the Ni is polycrystalline with a strong <111> texture in the growth direction. The Si layers were determined to be amorphous. At both the Ni-on-Si and Si-on-Ni interfaces an intermixed amorphous region 3 nm in width was found in the as-deposited sample.

A study conducted on phase-selection in Ni-Si multilayers during annealing by Wang et al. [88] indicated that in ion-beam deposited multilayers with a period of 4.78 nm,

a Ni-Si amorphous phase was the only phase containing Ni that formed in samples with 19, 25, or 64 at% Ni. Crystalline Ni was detected only in the multilayer which contained 75 at% Ni. A second set of multilayers with a larger bilayer period of 10.1 nm and an average composition of 49 at% Ni was also examined. In the larger bilayer samples cross-sectional TEM images revealed that an amorphous interfacial layer exists between the Si and Ni layers. From plan-view TEM samples, Ni crystallites were determined to be 3 nm in size. No measurement was given for the width of the interfacial regions, but information from the SAED patterns indicate that c-Ni, a-Si and a-(Ni, Si) were present.

In a later study by Wang et al. [88] of a Ni/Si multilayer with a bilayer period of 16.6 nm and average composition of 49 at% Ni there was no mention of any extensive intermixing at the interface. The Ni layer was described as polycrystalline with crystallite size estimated from LAXS data to be on the order of the layer width (5.7 nm). It was also mentioned that the crystallites were oriented in the growth direction.

## 1.8 Relevance of Previous Work to Present Study

The review of the past investigations of metal/silicon multilayers reveals that the multilayer structure observed during a TEM investigation may result from a variety of influences related to the deposition conditions, the component layer materials, the layer configurations, and possibly by the preparation of the TEM sample itself. The wide variety of deposition conditions studied in the Mo-Si multilayer investigations provides a basis from which one can relate the observed structure in the spin-glass multilayers to the sputtering conditions. From the several systems reviewed, it is also apparent that the existence of asymmetric (Mo-Si) or symmetric (Ti-Si) interface regions between the

alternating layers are intrinsically related to the component materials involved. Lastly, in many of the systems the occurrence of partial or complete amorphization of the metal layer (e.g. W-Si) appears to depend upon the metal involved and the intended layer thickness.

Since the ultimate goal of the finite-size studies of spin-glass materials is to relate spin-glass properties to the thickness of the pure material layer, it is important to understand the origin of the structural features and how they may be affected by both the deposition conditions and the preparation of the TEM cross-sections.

In the present study, an attempt is made to address the concerns of sample preparation artifacts by evaluating two different methods of TEM specimen preparation, ultramicrotomy and ion-milling. Unfortunately, not all the information provided by ion-milled HRTEM samples (e.g. interfacial mixing) is available from ultramicrotomed CTEM samples. However, some comparisons between the information provided by the CTEM and HRTEM samples, like the relative degree of crystallinity, can be made. Furthermore, it is also possible to compare the information derived from the electron microscopy with that obtained from the x-ray characterizations of the multilayers.

#### CHAPTER 2 EXPERIMENTAL PROCEDURES AND MATERIALS

## 2.1 Spin-Glass Multilayer Fabrication

The thin-film multilayers described in this study were synthesized by Dr. Lilian Hoines of the MSU Physics Department [18]. The examined multilayer thin-films were DC-magnetron sputtered onto [001] single-crystal silicon substrates (1 cm<sup>2</sup>) in an UHV compatible system operating at 1x10<sup>-6</sup> Pa with an argon sputtering pressure of 0.33 Pa. The substrates were cleaned in acetone and alcohol using an ultrasonic cleaner prior to loading into the sputtering apparatus. The sample substrate was cooled during deposition through direct contact with a oxygen free high conductivity Cu block. This block was thermally coupled with another component of the sputtering assembly which was cooled by a LN<sub>2</sub> reservoir. The alloy composition (in atomic percent), deposition rate, plasma voltage, and current for the three systems are listed in Table 2.1.

The multilayers used for spin-glass studies consisted of 3 nm or 7 nm layers of metal spin-glass alloy alternating with 7 nm layers of amorphous silicon (Figure 2.1). In the multilayers with 3 nm spin-glass layers, 67 bilayers (or pairs) of the metal spin-glass alloy and amorphous silicon layers were deposited to form a structure with a nominal total thickness of 670 nm. In the multilayers with 7 nm spin-glass layers, 29 bilayers of the metal spin-glass alloy and amorphous silicon layers were deposited to form a structure with a nominal total thickness of 406 nm. The number of bilayers for the samples of

Table 2.1 Sputtering parameters of spin-glass layers [18].

Target Material	Plasma Voltage (kV)	Plasma Current (ma)	Deposition Rate (A/sec)
Cu <sub>.85</sub> Mn <sub>.15</sub>	-400	0.70	12.7
Ag <sub>.91</sub> Mn <sub>.09</sub>	-400	0.75	6.8
Au <sub>.97</sub> Fe <sub>.03</sub>	-320	0.40	~6

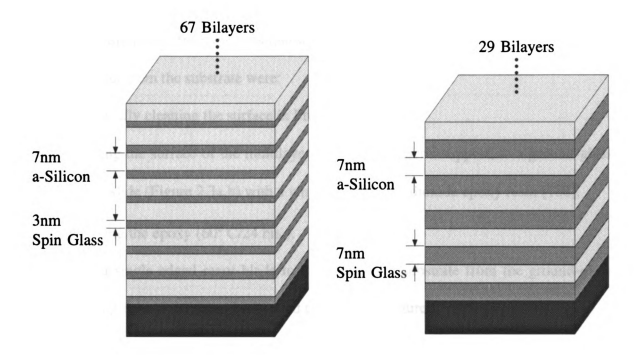


Figure 2.1 Multilayer sample configurations.

different spin-glass layer widths was calculated to provide an equivalent total amount of spin glass. <111> Diffraction peaks in the large angle x-ray scans (LAXS) of the multi-layers (Figure 2.2) indicated that all the specimens displayed some degree of crystallinity.

## 2.2 CTEM Specimen Preparation using Ultramicrotomy

To facilitate sample preparation for CTEM examination a mechanical method to remove the multilayer from the substrate was used [107]. The steps involved in separating the multilayer from the substrate were:

- 1) Ultrasonically cleaning the surface in Freon™ TF.
- 2) Cementing the surface of the multilayer, still on the silicon support, to a ground-glass microscope slide (Figure 2.3a,b) with a vinyl cyclohexane dioxide epoxy resin [108].
- 3) Heat curing the epoxy (60° C/24 hrs.).
- 4) Use of a single-edged razor blade to pry the silicon substrate from the ground-glass slide, leaving behind the thin-film bonded to the slide (Figure 2.3c,d).
- 5) Separating the multilayer thin-film from the slide by digesting the epoxy in a solution of sodium ethoxide in ethanol for 2-4 hours (Figure 2.3e).
- 6) Rinsing the freed film with ethanol followed by Freon™ TF.
- 7) Placing a small piece (1-2 mm<sup>2</sup>) into a silicone mold half-filled with polymerized epoxy resin (Figure 2.3f).

The multilayer thin-film was then covered by filling the mold with the same epoxy.

The epoxy was cured for a minimum of 12 hours at 60° C. Once the block had polymerized it was trimmed in the typical manner of ultramicrotomy preparation [109-115] to form a trapezoidal pyramid containing the multilayer thin-film. Ultrathin sections

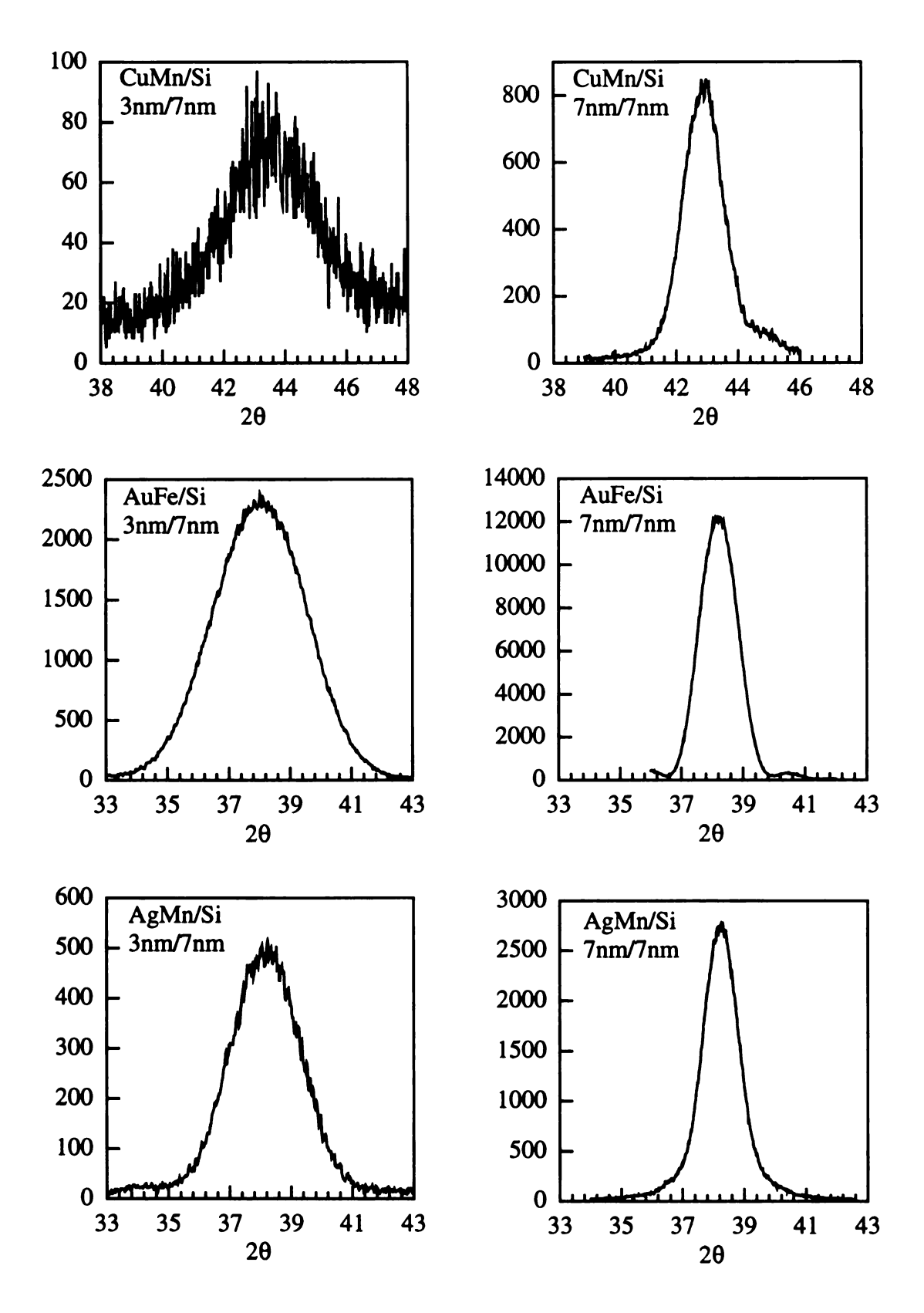


Figure 2.2 Large angle x-ray scans of <111> peaks in spin-glass multilayers. After Hoines [18].

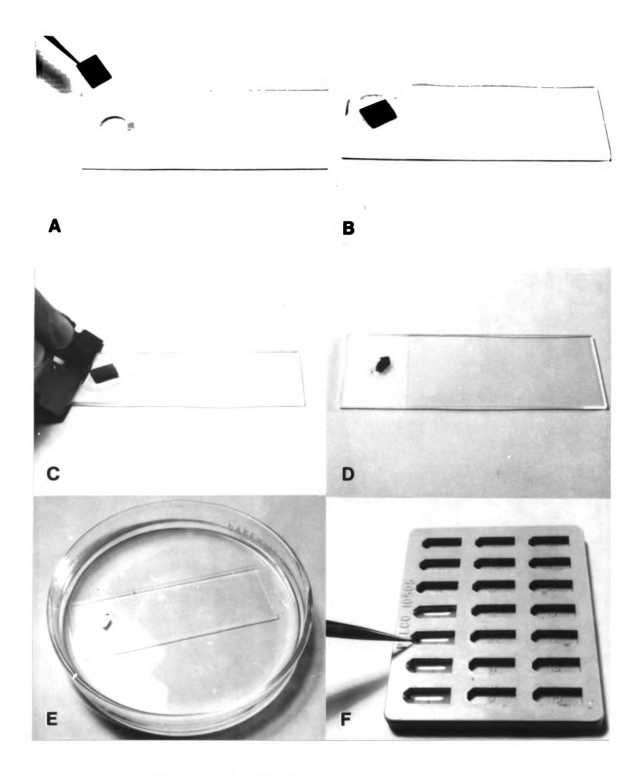


Figure 2.3 Multilayer removal from silicon substrate.

(50-70 nm) were then cut using a 55° diamond knife on a Reichert-Jung Ultracut microtome with a sectioning speed of 0.4 mm/sec. The microtomed sections were floated onto distilled water and collected on bare 1000 mesh Cu TEM grids (Figure 2.4). The specimens were then lightly carbon coated (to improve resin stability) and observed in a Hitachi H800 TEM operated at 200 kV. Provided that the two bonded surfaces were properly cleaned, the resultant bond of the thin-film to the ground-glass slide was stronger than the bond to the silicon substrate. Figure 2.5 shows a low-magnification bright-field image of the 1000 mesh Cu TEM grid along with a trapezoidal thin section containing the multilayer embedded in the epoxy. The loss of adhesion between the multilayer and the supporting epoxy resulted in the formation of the corkscrew structure indicated by arrow A in Figure 2.6. In many of the ultrathin sections the multilayer still adhered to the resin on at least one side, and remained flat (arrow B, Figure 2.6). Electron transparent cross-sections were observed over lengths as great as 500 μm.

## 2.3 HRTEM Specimen Preparation

Although the method for preparing CTEM specimens provided samples suitable for a quick and complete survey of the multilayer structure, samples prepared in this manner did not allow HRTEM observations because of the thickness of the resultant cross-sections. Two different methods involving ion-milling were evaluated for obtaining cross-section specimens suitable for HRTEM imaging. Both methods involved the fabrication of a composite slab by using epoxy to join two cut pieces of the multilayer face-to-face [116]. This slab was then either encased within a slotted rod and tube [117-121] or epoxied onto a molybdenum ring (Figure 2.7). The procedure to form the composite slab

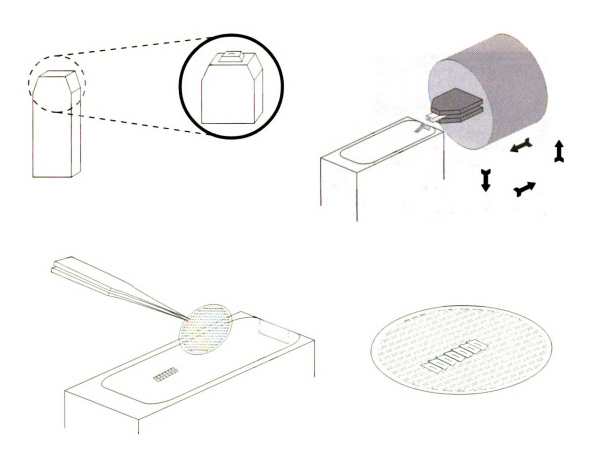


Figure 2.4 Sequence for ultramicrotomy sectioning and collecting ultrathin sections.

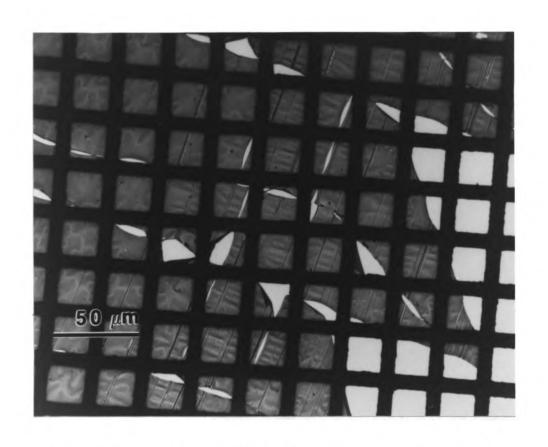


Figure 2.5 Low magnification CTEM of ultrathin sections on grid.

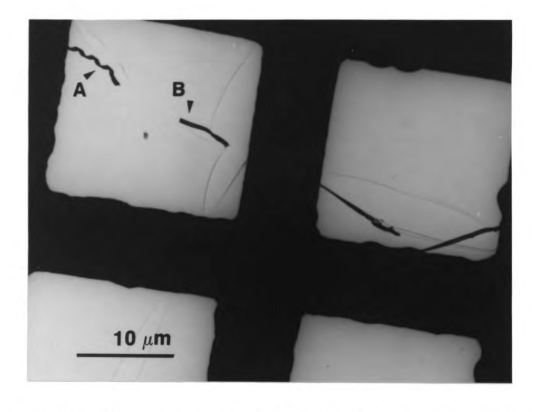


Figure 2.6 Higher magnification CTEM of multilayer embedded in epoxy resin.



Figure 2.7 Composite slab, slotted-rod, tube, and molybdenum rings.

#### was as follows:

- 1. Cut multilayer sample on substrate into 2.5 mm slabs.
- 2. Clean slabs in acetone followed by a rinse with Freon™ TF.
- 3. Place one slab with multilayer face up in the slotted Teflon™ block vice.
- 4. Cover slab with a thin coating of Gatan<sup>™</sup> G-1 epoxy.
- 5. Place second slab with multilayer face down on top of first slab.
- 6. Tighten vice to compress slabs together and place in drying oven at 60° C.
- 7. Cure epoxy for 90 mins.

For the slotted-rod and tube method the composite slabs were coated with Gatan<sup>™</sup> G-1 epoxy and placed within the slot of the rod, which was subsequently coated with epoxy and place inside the tube. The whole assembly was then cured on a hot plate for 90 minutes at 75° C. The assembly was then diced into 800 μm thick sections with a low-speed diamond saw (Figure 2.8). The 800 µm thickness was found to be optimal since it allowed for any sectioning damage on both sides of the cut disc to be ground away without affecting the final exposed sample surface. The individual discs were attached with Crystalbond™ to Pyrex™ stubs which fit into the Disc Grinder (Figure 2.9 and 2.10). The use of the Disc Grinder allowed the discs to be polished to a thickness of 100 µm while maintaining parallel top and bottom surfaces. The sequence of diamond pastes used was 15, 9, 6, 3, 1, 0.5 µm on a nylon cloth covered stationary lap wheels. After the final polishing, the sample and stub were transferred to a Gatan™ Precision Dimple Grinder (Figure 2.11). The discs were dimpled using a 15 mm diameter brass dimpling wheel [122,123]. Both sides were dimpled to an approximate depth of 40 µm. The final dimpling depth was monitored by removing both the sample and stub and placing the

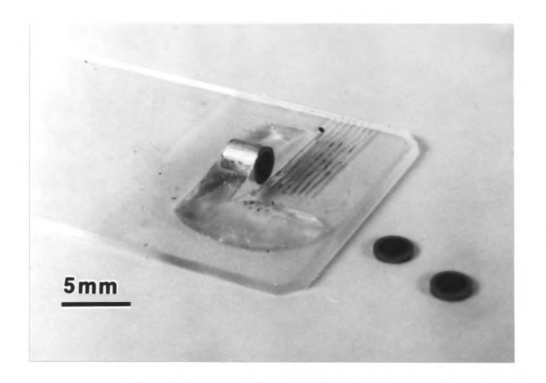


Figure 2.8 Sectioned discs of slotted-rod and tube specimen.

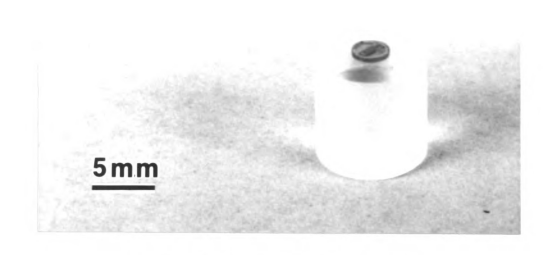


Figure 2.9 Sectioned disc on Pyrex<sup>TM</sup> stub.



Figure 2.10 Sectioned disc and stub in Gatan™ Disc Grinder.



Figure 2.11 Dimpler wheel and TEM specimen on Pyrex™ stub.

assembly on a transmitted light microscope. At thicknesses less than 10  $\mu$ m the silicon substrate will transmit red light [124]. It was found, however, that the samples would have a tendency to crack before this thickness was reached due to a lack of dampening control on the dimpler. It was determined that the best way to monitor depth was to calculate the depth using the approximation,  $d = r^2/D$ , relating the diameter of dimple (2r) and wheel diameter (D) to dimple depth (d). The dimple diameter was measured under the microscope using a calibrated graticule. Based on the amount of material removed, the estimated thinnest portions of the discs prior to ion-milling ranged between 20 and 50  $\mu$ m. Once the sample was dimpled the disc was released from the specimen stub by soaking in acetone to dissolve the Crystalbond<sup>TM</sup>. The final thinning to electron transparency was done with a cold-stage Ar<sup>+</sup> ion-mill operating at 5 kV and a beam current of 1 ma [125-128]. Initial milling was done at 45 degrees until perforation, then at 15 degrees until samples were thin enough for HRTEM observations. An SEM image of a typical TEM specimen illustrates the final sample geometry after ion-milling (Figure 2.12)

Another method used for HRTEM cross-sections was the slab-on-ring method developed by Romano et al. [129, 130] and Shaapur and Park [131]. In this method the composite slabs were sectioned into 800 µm pieces (Figure 2.13). The individual pieces were temporarily attached to Pyrex<sup>TM</sup> stubs to allow polishing of the cross-section interface. After polishing one side, the slab was removed and the polished face was attached to a TEM Molybdenum support ring with Gatan<sup>TM</sup> G1 epoxy. The curing was done on a hot plate using an 8 mm thick piece of Teflon<sup>TM</sup> to prevent attachment of the slab and ring to the hot plate itself. The slab and ring were then reattached to the Pyrex<sup>TM</sup> stub with Crystalbond<sup>TM</sup>. The second side of the slab was then polished to final slab thickness of

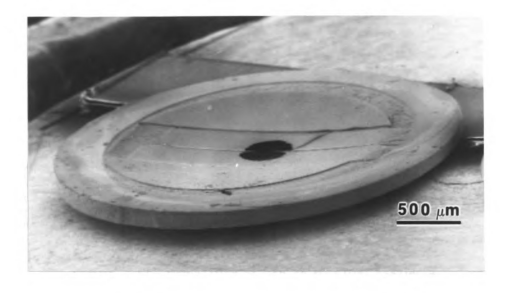


Figure 2.12 SEM image of TEM specimen after dimpling and ion-milling.

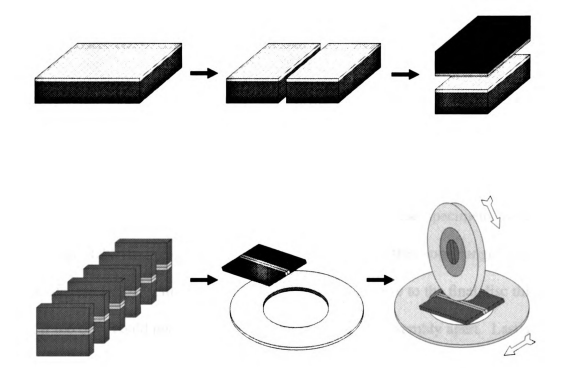


Figure 2.13 Fabrication of slab-on-ring type specimen.

100 µm, excluding the 50 µm thickness of the Mo-ring. These samples were dimpled only from the top surface. The dimpling procedure was the same as for the method previously described. Final thinning with the ion-mill was the same as well. HRTEM images of the multilayer samples were obtained using a JEOL 4000EX operating at 400 kV. HRTEM images were recorded with the objective lens close to Scherzer defocus in order to maximize image contrast [132]. The HRTEM was performed at the Electron Microbeam Analysis Laboratory (EMAL) located at the University of Michigan, Ann Arbor, MI.

Light microscope images of the slotted-rod/tube and slab-on-ring type TEM specimens are show in Figure 2.14. Although the slotted-rod/tube specimens were more mechanically stable they did have several drawbacks. One, they took longer to prepare then the slab-on-ring specimens. Two, they were also sensitive to the final disc thickness which, if too thin, could result in the outer ring torquing the assembly apart. Lastly, if the stainless steel rod material experienced enough mechanical working it would become slightly magnetic. This caused significant problems when attempting to correct the astigmatism of the objective lens in the microscope used for HRTEM work. Thus, all of the HRTEM cross-sections were of the slab-on-ring type. Both sample types, however, suffered from the effects of differential ion-milling. This effect was due to the vastly different ion-milling properties of the crystal silicon substrate and the multilayer thin film. The result of the less-resistant silicon milling away faster was the formation of needle-like projections containing the electron transparent multilayer areas extending over the hole (Figure 2.15).

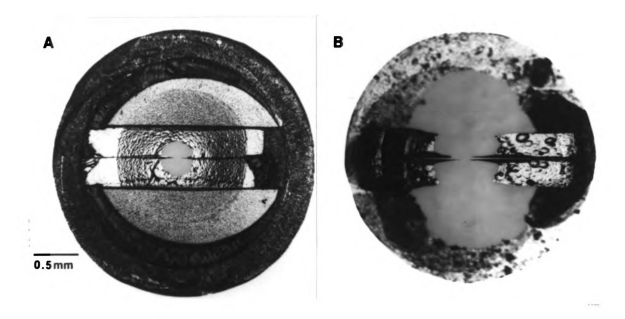


Figure 2.14 a) Slotted-rod and tube b) slab-on-ring specimen configurations.

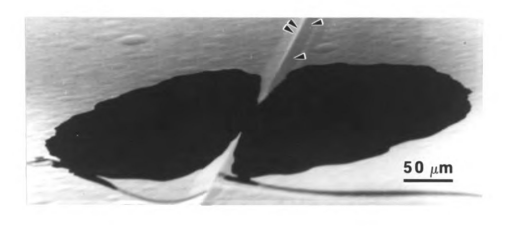


Figure 2.15 SEM image of differential milling at multilayer/substrate interface.

#### CHAPTER 3 EXPERIMENTAL RESULTS

#### 3.1 CTEM of Microtomed Multilayers

## Au 97Fe 03/Si Multilayers

Microtomed sections observed with CTEM provided useful information about the uniformity and continuity of layering in the multilayers. The sections were also useful in detecting the presence of crystal texture in the spin-glass layers using SAED techniques. Figure 3.1 shows a microtomed multilayer composed of 3 nm Au<sub>.97</sub>Fe<sub>.03</sub> layers (dark contrast material) and 7 nm silicon layers (light contrast material). What is apparent from the bright field CTEM image is that the relative widths of the two materials do not correspond to the intended fabrication parameters. The discrepancy can be explained as a contrast artifact which occurs in thick cross-sections (> 50 nm) of multilayers which also contain an amorphous silicon layer [133]. This problem is also apparent in a microtomed section of multilayer which is suppose to contain equal 7 nm layers of Au<sub>.97</sub>Fe<sub>.03</sub> and silicon (Figure 3.2). The disparity in apparent layer widths may be further exacerbated due to a misalignment of the layer interfaces with respect to the beam as indicated by the superlattice reflections missing from the 5 and 11 o'clock positions in the SAED pattern (Figure 3.2 inset). From the SAED insets in both Figures 3.1 and 3.2 one can observe a change in texture between the 3 nm/7 nm and 7 nm/7 nm Au<sub>.97</sub>Fe<sub>.03</sub>/Si multilayers. In the 3 nm/7 nm Au<sub>.97</sub>Fe<sub>.03</sub> multilayer a diffuse ring exists at the Au<111> reflection indicating a

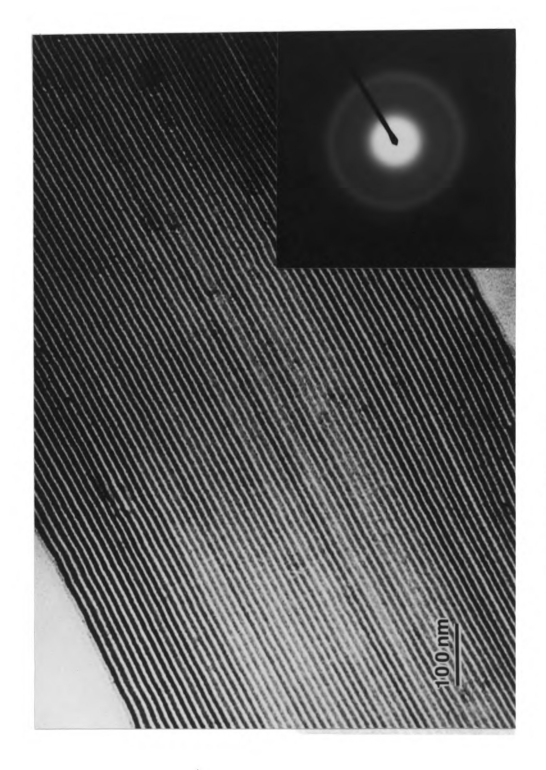


Figure 3.1 CTEM of Au<sub>.97</sub>Fe<sub>.03</sub>/Si 3 nm/7 nm multilayer.

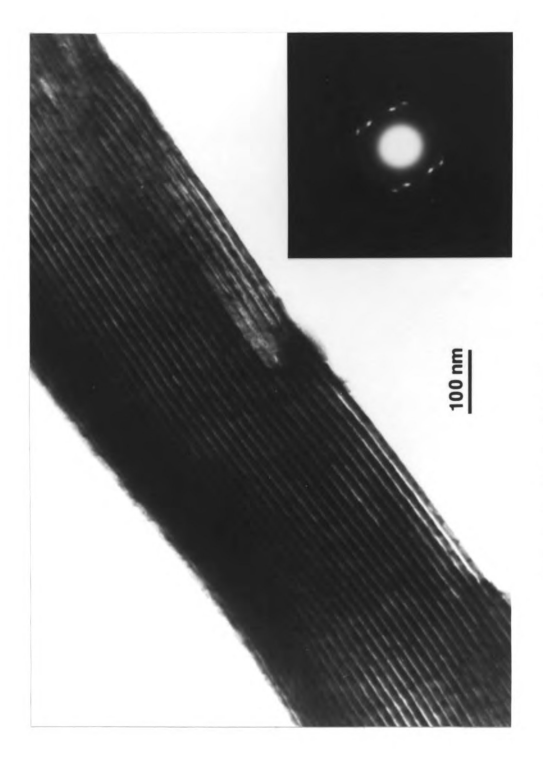


Figure 3.2 CTEM of Au<sub>.97</sub>Fe<sub>.03</sub>/Si 7 nm/7 nm multilayer.

microcrystalline or amorphous material (Figure 3.1 inset). This is in contrast to the multilayer with the thicker 7 nm Au<sub>.97</sub>Fe<sub>.03</sub> spin glass layer which has a SAED pattern indicating a distinct <111> texture (Figure 3.2 inset). One other interesting aspect of the 3 nm/ 7 nm Au<sub>.97</sub>Fe<sub>.03</sub>/Si multilayer was the ability to induce crystallization with the electron beam of the microscope. Figure 3.3 is a CTEM bright-field/dark-field pair of the same multilayer sample in Figure 3.1 after condensing the beam to cross-over. Once cross-over occurs, darker contrasting material coalesces into 70-300 nm regions, some with boundaries following the initial layering. The SAED inset of Figure 3.3a shows that the material has become more strongly crystallized than before the reaction (Figure 3.1 inset). Dark field imaging of the altered multilayer reveals that the crystallites have sizes ranging from 30 nm-700 nm. This reaction was induced in only the 3 nm/7 nm Au<sub>.97</sub>Fe<sub>.03</sub>/Si sample. This unique behavior could be ascribed to either the properties of the multilayer itself (individual layer thickness, interfacial mixing) or aspects of the particular TEM specimen (sample heating due to poor thermal or electrical conductivity).

## Cu 85Mn 15/Si Multilayers

Figure 3.4 is a bright-field image of a Cu<sub>.85</sub>Mn<sub>.15</sub>/Si 3 nm/ 7nm multilayer. The microtomed cross-section reveals that the layering is uniform and continuous. The cross-section, however, does display some curling at the edges which causes some of the image to be distorted. The bright area which is in the same focal plane illustrates that the layering is free from any progressive interface roughness. The diffuse SAED pattern (Figure 3.4 inset) indicates that the spin-glass layers are either microcrystalline or amorphous. Figure 3.5 is a bright-field image of a multilayer with the same composition as the one in

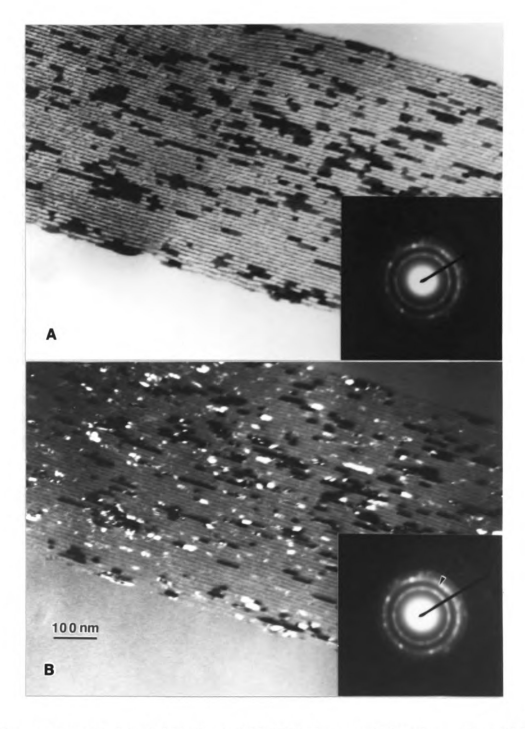


Figure 3.3 a) Bright-field b) Dark-field CTEM images of altered Au. $_{97}$ Fe  $_{03}$ /Si 3 nm/7 nm multilayer.

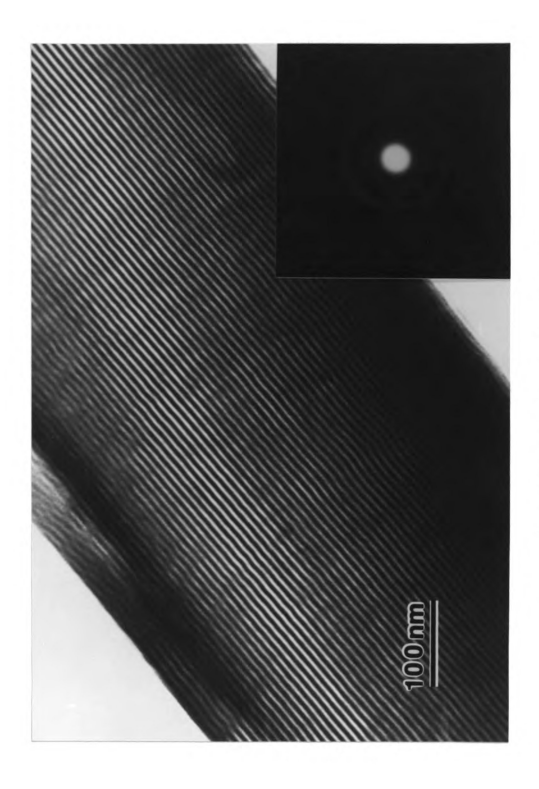


Figure 3.4 CTEM of Cu<sub>.85</sub>Mn<sub>.15</sub>/Si 3 nm/7 nm multilayer.

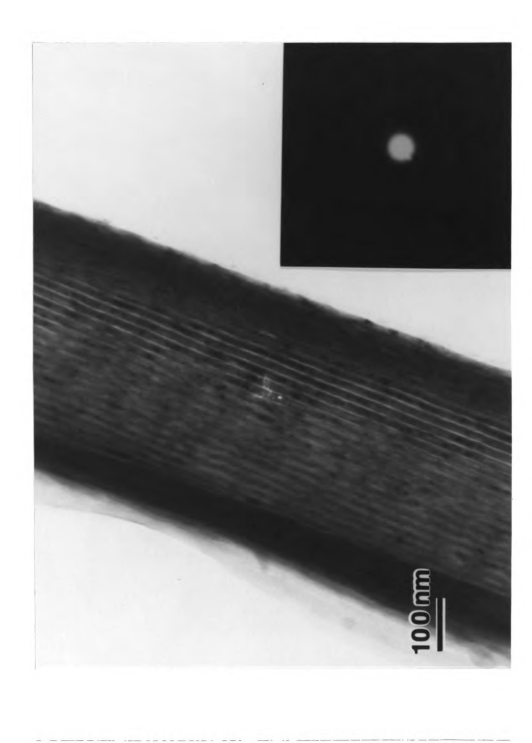


Figure 3.5 CTEM of Cu<sub>.85</sub>Mn<sub>.15</sub>/Si 7 nm/7 nm multilayer.

Figure 3.4 but with a thicker 7 nm spin-glass layer. In the areas oriented properly with no material curled underneath it is possible to discern straight uniform layers. The thickness of the specimen, however, gives rise to the contrast artifact that makes the amorphous layer width appear smaller. From the SAED pattern (Figure 3.5 inset) a slight texture is apparent in the diffraction ring.

# Ag 91Mn 09/Si Multilayers

Figure 3.6 is a CTEM bright-field image of a Ag<sub>.91</sub>Mn<sub>.09</sub>/Si multilayer with a 3 nm spin-glass layer and a 7 nm silicon layer. The curling in this film produces some distortions in the image near the edges, but the areas in focus do reveal that the layering is continuous and uniform. The apparent widths of the two different component layers are closer to the expected relative widths, which indicates that the microtomed sample may be thinner and the effects of the contrast artifact lessened. From the SAED inset of Figure 3.6 it is observed that the spin-glass layer is well crystallized and has a strong texture. Figure 3.7 is a CTEM bright-field image of a multilayer with the same spin-glass composition as in Figure 3.6 but with a thicker spin-glass layer. From the bright-field image it is possible to discern the layering in only a portion of the multilayer due to surface contamination of the microtomed section (possibly curled over embedding epoxy). As in the other 7 nm thick spin-glass layer materials, the apparent width of the silicon layer does not appear to be equivalent to that of the spin-glass layer. The SAED inset of Figure 3.7 indicates that the Ag<sub>.91</sub>Mn<sub>.09</sub>/Si multilayer with the 7 nm thick spin-glass layer is as well-crystallized and textured as the Ag<sub>.91</sub>Mn<sub>.09</sub>/Si multilayer with the 3 nm thick spin-glass layer.

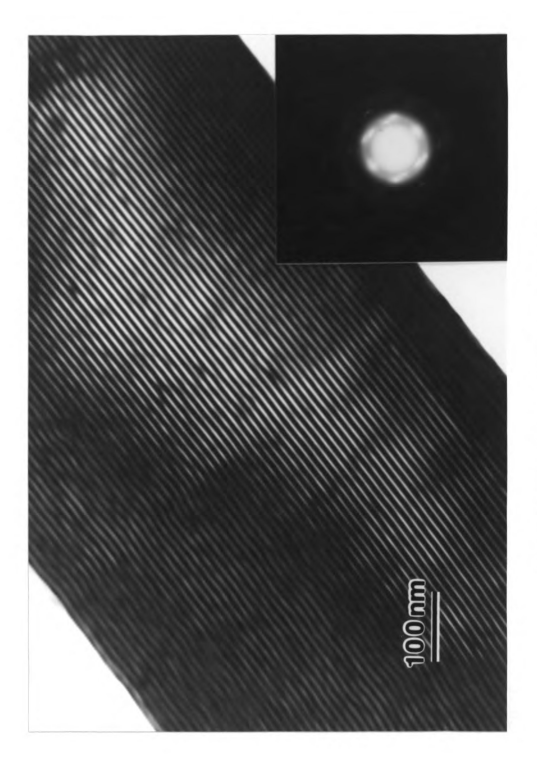


Figure 3.6 CTEM of Ag.91Mn.09/Si 3 nm/7 nm multilayer.



Figure 3.7 CTEM of Ag.91Mn.09/Si 7 nm/7 nm multilayer.

#### 3.2 HRTEM of Ion-Milled Multilayers

# Cu<sub>.85</sub>Mn<sub>.15</sub>/Si Multilayers

While CTEM was useful for confirming continuous and uniform layering it was of limited use in distinguishing between microcrystalline and amorphous material layers and the amount of interdiffusion between the two layers. Figure 3.8a shows several bilayers of the Cu<sub>.85</sub>Mn<sub>.15</sub>/Si 7 nm/7 nm multilayer, where the dark regions are the spin-glass layers and the lighter regions are the amorphous silicon. It is clear that the layer widths are continuous and relatively uniform. However, it appears that the apparent width of the amorphous silicon layer does not correspond to an equal width of the Cu<sub>.85</sub>Mn<sub>.15</sub> spin-glass layer. An enlarged area of the image (Figure 3.8b) shows the details of this structure. Note that the spin-glass layers show a large degree of crystallinity, as evidenced by the distinct lattice structure imaged in many areas of these layers. This lattice structure image was obtainable due to the strong [111] fiber texture of the polycrystalline films. In contrast, the silicon layers are clearly amorphous, with no periodicity in the structure. Additionally, Figure 3.8b reveals that a significant portion of the amorphous silicon is mixed with the outer atomic layers of the spin-glass material on both the top and bottom interfaces, giving rise to an intermixed region of intermediate contrast.

A HRTEM image of a multilayer with the same Cu<sub>.85</sub>Mn<sub>.15</sub> spin-glass composition as in Figure 3.8, but with thinner spin-glass layers is shown in Figure 3.9a. In this multilayer the relative widths are closer to the intended fabrication thicknesses of 3 nm of spin-glass and 7 nm of amorphous silicon. One interesting feature of the multilayer with the thinner spin-glass layers is that it appears to be amorphous throughout. An enlarged area of the multilayer (Figure 3.9b) typifies the apparent amorphous structure.

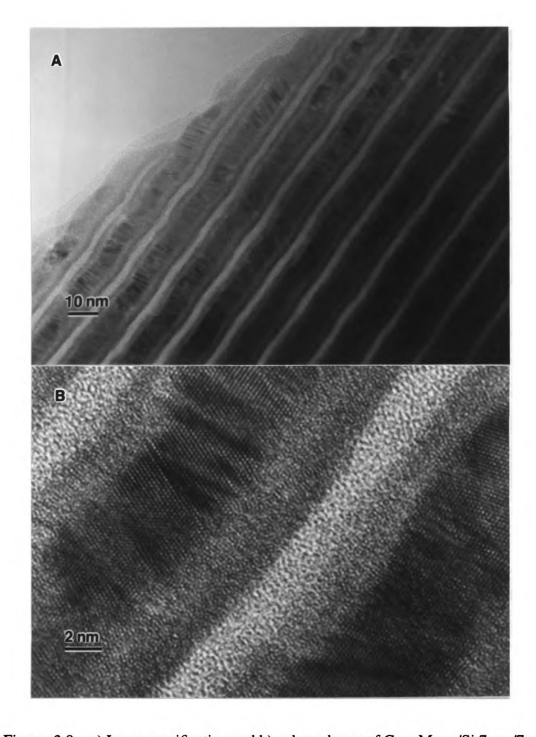


Figure 3.8 a) Low magnification and b) enlarged area of  $Cu_{.85}Mn_{.15}/Si~7~nm/7~nm$  multilayer.

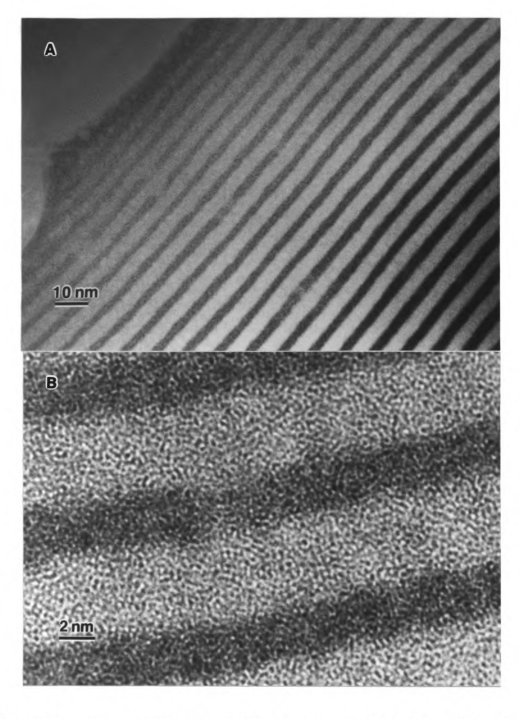


Figure 3.9 a) Low magnification and b) enlarged area of  $Cu_{.85}Mn_{.15}/Si~3~nm/7~nm$  multilayer.

### Au 97Fe 03/Si Multilayers

A HRTEM image of a Au<sub>.97</sub>Fe<sub>.03</sub>/Si 7 nm/7 nm multilayer is shown in Figure 3.10a. It is evident that the layers are continuous and maintain a uniform bilayer periodicity. Problems associated with differential ion-milling resulted in only one layer that was thin enough for lattice imaging. Nonetheless, it is possible to observe asymmetry in the interfacial regions. The Au<sub>.97</sub>Fe<sub>.03</sub>-on-Si intermixing region is thicker than the Si-on-Au<sub>.97</sub>Fe<sub>.03</sub> region. An enlarged area (Figure 3.10b) shows the Au<sub>.97</sub>Fe<sub>.03</sub>-on-Si interface and reveals that a portion of the Au<sub>.97</sub>Fe<sub>.03</sub> layer is well-crystallized. The multilayer in Figure 3.11a also contains a Au<sub>.97</sub>Fe<sub>.03</sub> spin-glass, but with a 3 nm spin-glass layer and a 7 nm amorphous silicon layer. The round patches which span both layers are the result of redeposited ion-milled silicon substrate material. The details of the interface between the Au<sub>.97</sub>Fe<sub>.03</sub> spin-glass and the amorphous silicon are shown in Figure 3.11b. The lack of any significant intermixing is perplexing in light of the presence of an intermixing region in the thicker spin-glass layers. It is possible that variations in deposition parameters or sample preparation conditions could account for the absence of intermixing regions.

## Ag<sub>.91</sub>Mn<sub>.09</sub>/Si Multilayers

Figure 3.12a is a HRTEM image of the Ag<sub>.91</sub>Mn<sub>.09</sub>/Si multilayer with intended 3nm spin-glass and 7 nm amorphous silicon layers. This particular specimen illustrates the consequences of differential ion-milling where the crystalline silicon substrate (lower right corner) has thinned preferentially, allowing a lattice structure image of the substrate but not of the multilayers. In Figure 3.12b, lattice fringes can be observed in the center of the spin-glass layer. The intermediate contrast edges on both sides of the Ag<sub>.91</sub>Mn<sub>.09</sub> layer

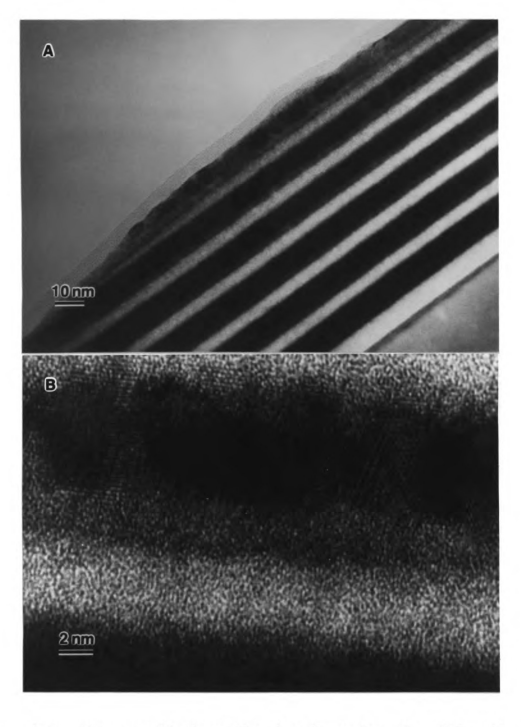


Figure 3.10 a) Low magnification and b) enlarged area of Au  $_{97}{\rm Fe}_{.03}/{\rm Si}$  7 nm/ 7 nm multilayer.

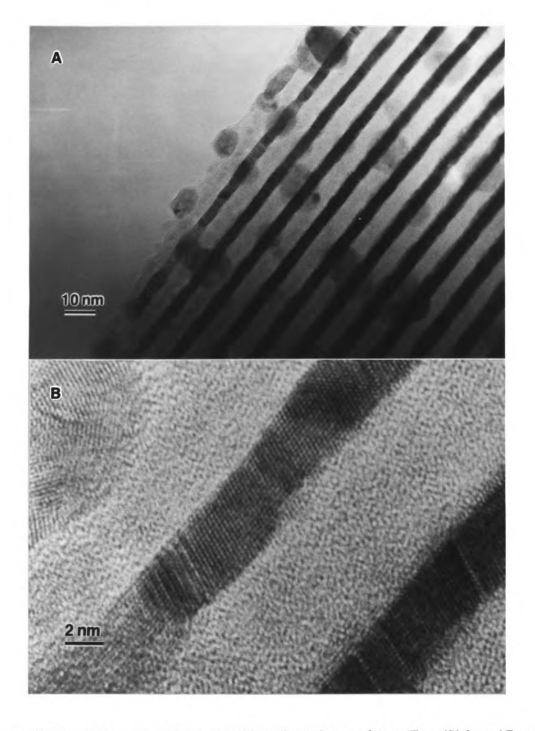


Figure 3.11 a) Low magnification and b) enlarged area of  $Au_{.97}$ Fe  $_{.03}$ /Si 3 nm/ 7 nm multilayer.

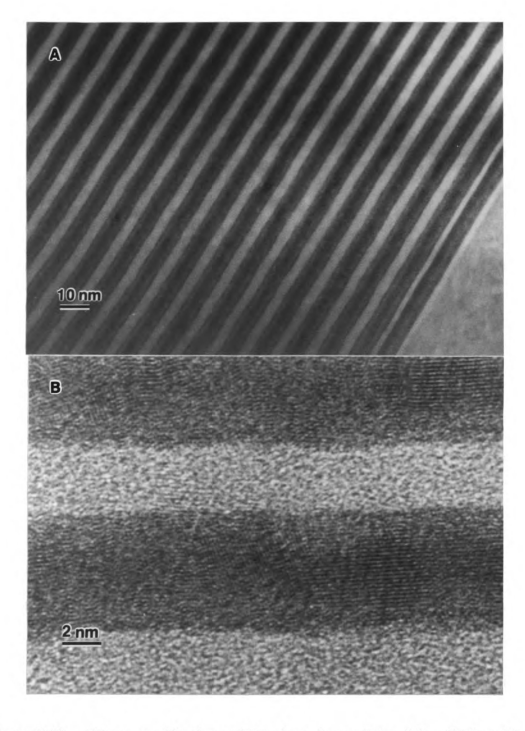


Figure 3.12 a) Low magnification and b) enlarged area of  $Ag_{.91}Mn_{.09}/Si~3~nm/7~nm$  multilayer.

suggest some intermixing at the interfaces. The thickness of the specimen, however, precludes the characterization of interfacial layer width.

#### 3.3 TEM and X-ray Characterization of Bilayer Periodicity.

In addition to the characterization of the uniformity and interfacial structure of the spin-glass layers, the use of cross-sectional TEM allowed a determination of the bilayer periodicity of the multilayers. These measurements could then be compared to the values determined from small-angle x-ray scans [18]. Figure 3.13 is a small-angle x-ray scan of the Au<sub>.97</sub>Fe<sub>.03</sub>/Si 7 nm/ 7nm multilayer [18]. The pairs of layers with a constant bilayer thickness form a periodic structure capable of producing Bragg reflections with very small 2Θ values. The multiple peaks shown in figure 3.13 result from higher orders of the reflection from the bilayer periodicity. It is possible to derive the bilayer periodicity from the spacing of the higher order reflections based on a derivation of Bragg's law which incorporates the index of refraction of x-rays [18]. Results of the SAXS determination of bilayer periodicity are listed in Table 3.1.

The determination of the bilayer periodicity from TEM cross-sections was accomplished by digitizing images enlarged from HRTEM negatives. Line scans of image contrast differences across the four layers nearest the substrate were used to measure the bilayer periodicity. The measurements on the images were calibrated using the 0.314 nm <111> lattice spacing of the crystal silicon substrate. Results for five of the six samples are listed in Table 3.1. No HRTEM results where obtained for the Ag<sub>.91</sub>Mn<sub>.09</sub>/Si 7 nm/ 7 nm sample and it was not possible to obtain an accurate periodicity from the CTEM images since they lacked a silicon lattice image to use as an internal calibration.

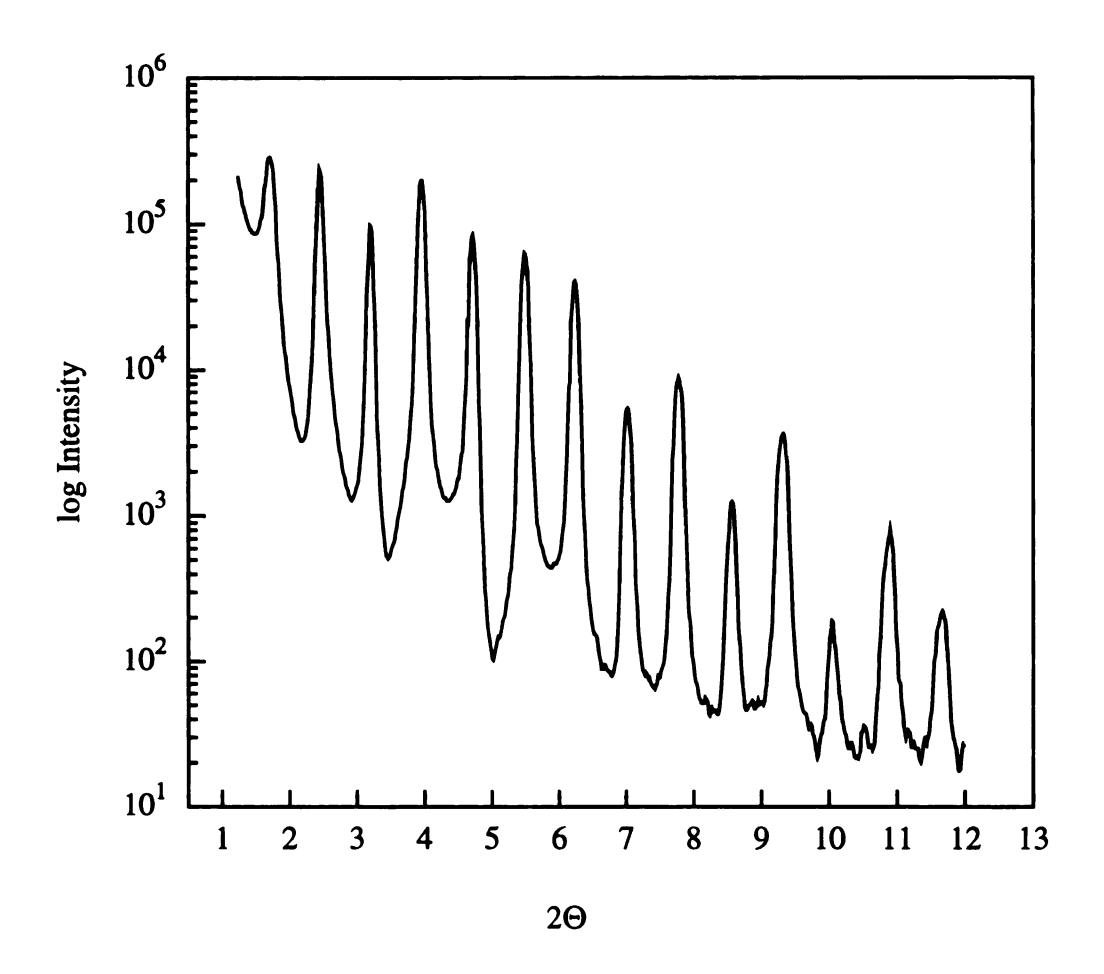


Figure 3.13 Small-angle x-ray scan of Au<sub>.97</sub>Fe<sub>.03</sub>/Si 7 nm/7 nm multilayer. After Hoines [18]

Table 3.1 Bilayer periodicity in spin-glass multilayers.

Spin-Glass Multilayer Composition & Configuration	Bilayer Period from SAXS (nm)	Bilayer Period from HRTEM (nm)
Cu <sub>.85</sub> Mn <sub>.15</sub> /Si 3 nm/7 nm 67 bilayers	10.02	8
Cu <sub>.85</sub> Mn <sub>.15</sub> /Si 7 nm/7 nm 29 bilayers	14.50	15
Au <sub>.97</sub> Fe <sub>.03</sub> /Si 3 nm/7 nm 67 bilayers	10.25	11
Au <sub>.97</sub> Fe <sub>.03</sub> /Si 7 nm/7 nm 29 bilayers	14.60	14
Ag <sub>.91</sub> Mn <sub>.09</sub> /Si 3 nm/7 nm 67 bilayers	11.12	10

Four of the five systems for which bilayer measurements where made using the HRTEM images show reasonable agreement with the SAXS results. Differences between the two methods may reflect the effect of local interfacial roughness in the HRTEM measurements, especially if asymmetric interfacial regions were present. A comparison of the values for bilayer periodicity determined from the two methods reveals poor agreement between the results for the Cu<sub>85</sub>Mn<sub>15</sub>/Si 3 nm/7 nm multilayer. This discrepancy is difficult to explain by the possible alteration of the multilayer from ion-milling damage since such damage would only affect the width of the spin-glass layer relative to the amorphous silicon layer. One possible explanation could be the fact that only HRTEM images of the bilayers near the substrate were used in order to maintain the calibration of the silicon lattice. Therefore, the measurements were not averaged over as many bilayers as in the SAXS measurements. One other concern was the possibility that a  $Cu_{.85}Mn_{.15}/Si$  sample with a different bilayer configuration was inadvertently provided as a 3 nm/7 nm multilayer. Since the TEM sample preparation is a destructive technique it was not possible to repeat the SAXS measurements.

#### CHAPTER 4 DISCUSSION

### 4.1 Experimental Factors Which Complicate Image Interpretation

In characterizing the presence of interfacial mixing in these multilayers no attempt has been made to make direct correlations of optical density of the micrographs with composition of the interlayer, since some of the image contrast will result from amplitude modulations in a thick higher Z specimen [134]. However, the contrast differences between pure amorphous silicon layers and the intermixed regions were sufficient to allow nominal estimates of the extent and symmetry of the intermixed regions based on the assumption that the areas of lowest contrast are pure silicon and that the crystalline regions are pure spin-glass material. Even with this simple interpretation there are experimental factors which can affect the apparent width of the interlayer and the pure component layers. These include defocus settings of the objective lens, sample tilting, and ionmill damage. Cheng et al. [56] made detailed characterizations of the apparent layer widths of the pure Mo and Si layers and their corresponding interlayers as a function of objective lens defocus. They determined that when the objective lens is further defocused from optimal or Scherzer defocus, the apparent width of Mo layers increased along with a corresponding decrease in the pure Si layer. The amount of defocus responsible for this effect was less than 100 nm, well below the amount where significant Fresnel fringes occurred (> ± 280 nm). The determination of the exact amount of defocus for the

spin-glass/amorphous HRTEM images was not determined, so some uncertainty exists in the apparent widths.

Cheng et al. also illustrated the effect of small amounts of sample tilt away from an orientation where the beam is parallel to the layering. They showed that the more strongly diffracting Mo crystallites made the layers containing them appear wider when the sample was tilted as little as 1.2°. Even with the initial orienting of the spin-glass layers parallel to the electron beam using the superlattice reflections around the zero-order spot, the possibility for misalignment exists in this study because of the local orientation variations along the milled edge of the multilayer as the thinned area is traversed.

Lastly, the effect of extensive ion-milling must also be addressed because of the possible alteration of the apparent layer widths due to interdiffusion during milling [56, 58]. Variations in sample geometry (slab thickness before dimpling, and final dimple depth) could affect the intensity of the ion-milling at the multilayer and may be responsible for increased sample heating. Despite the fact that a LN<sub>2</sub> cold-stage was used during milling, the needle-like projections (Figure 2.15) which resulted from the differential milling of the crystalline silicon substrate could have compounded the sample heating due to decreased heat dissipation. This effect may be particularly applicable to the 3 nm/7 nm Cu<sub>.85</sub>Mn<sub>.15</sub>/Si which appeared to be completely amorphous throughout the multilayer structure.

### 4.2 Crystallinity and Interlayer Mixing in Multilayers

With the effects of sample preparation and instrument parameters recognized, there are still some conflicting observations concerning the structural state of the

spin-glass layers (Table 4.1). Most notable is the disparity of the CTEM and the corresponding HRTEM images of the Au<sub>.97</sub>Fe<sub>.03</sub>/Si 3 nm/7 nm multilayers. The diffuse nature of the SAED pattern from the CTEM sample suggested that the spin-glass material was either poorly crystallized or amorphous. The HRTEM images, however, revealed that the spin-glass layers are highly crystalline. Although it was observed that the microtomed sections of Au<sub>.97</sub>Fe<sub>.03</sub>/Si used for CTEM could crystallize with electron beam heating, the effect of extensive ion-milling during HRTEM sample preparation usually induces amorphization [128]. One factor which has not been investigated very thoroughly is the long term stability of the multilayers at ambient temperatures. The period between the original CTEM investigation and the subsequent HRTEM study (~1.5 yr) may be significant.

The other discrepancy related to the Au<sub>.97</sub>Fe<sub>.03</sub>/Si system is the presence of intermixing at the interface for the 7 nm/7 nm multilayer configuration and the absence of such behavior in the 3 nm/7 nm sample. The lack of intermixing in the 3 nm/7 nm samples is problematic if one attempts to apply the mechanism of interfacial mixing proposed by Petford-Long et al. [39] which suggested that the relative difference in momentum of the sputtered elements having large differences in atomic weight is responsible for asymmetric intermixing regions.

With the exception of the 3 nm/7 nm Au<sub>.97</sub>Fe<sub>.03</sub>/Si sample, however, all HRTEM images of the other spin-glass samples did show evidence of interlayer mixing which was either symmetric (Cu<sub>.85</sub>Mn<sub>.15</sub>/Si 7 nm/7 nm, Ag<sub>.91</sub>Mn<sub>.09</sub>/Si 3 nm/7 nm) or asymmetric (Au<sub>.97</sub>Fe<sub>.03</sub>/Si 7 nm/7 nm). In addition to the aforementioned momentum argument for an as-deposited intermixing asymmetry, several researchers have proposed both kinetic and thermodynamic models for the results of in-situ and ex-situ annealing studies [29-35]

Table 4.1 Comparison of degree of spin-glass crystallinity from different methods.

Multilayer Composition and Configuration	LAXS	СТЕМ	HRTEM
Cu <sub>.85</sub> Mn <sub>.15</sub> /Si 3 nm /7 nm 67 bilayers	broad, low- intensity diffraction peak	SAED appears amorphous	Phase contrast image suggest amorphous spin-glass layer
Cu <sub>.85</sub> Mn <sub>.15</sub> /Si 7 nm /7 nm 29 bilayers	narrow, well- defined peak	SAED shows slightly textured, sharp rings	Phase contrast image reveals intermixed layer and crystalline spin-glass
Au <sub>.97</sub> Fe <sub>.03</sub> /Si 3 nm /7 nm 67 bilayers	broad, but well-defined peak	SAED appears amorphous	Phase contrast image indicates highly crystalline spinglass but no intermixed layer
Au <sub>.97</sub> Fe <sub>.03</sub> /Si 7 nm /7 nm 29 bilayers	narrow, well- defined peak	SAED shows highly textured, sharp arcs	Phase contrast image shows asymmetric intermixed layer and crystalline spinglass
Ag <sub>.91</sub> Mn <sub>.09</sub> /Si 3 nm /7 nm 67 bilayers	broad, but well-defined peak	SAED shows highly textured, sharp arcs	Phase contrast images reveals intermixed layer and crystalline spin-glass
Ag <sub>.91</sub> Mn <sub>.09</sub> /Si 7 nm /7 nm 29 bilayers	narrow, well- defined peak	SAED shows highly textured, sharp arcs	No result

which may be applicable to samples that have experienced heating during their preparation. Annealing studies of several metal-silicon multilayer systems, Mo-Si [42-45], Ti-Si [43, 45, 69, 73], Ni-Si [84-90], Al-Si [78, 93-95], Co-Si [45,70], have shown that two distinct types of systems exist, reactive and non-reactive. A reactive system, when annealed, will undergo a solid-state amorphization reaction [29]. What is observed during the anneal is the planar growth of the as-deposited amorphous intermixed layer such that any original crystalline material in metal layer is consumed by the formation of amorphous silicide. This behavior has been demonstrated in Ti-Si [69], using rapid thermal annealing techniques (450° C for 30 s). It was shown that the crystalline Ti layers which had symmetrical intermixing on both the Ti-on-Si and Si-on-Ti interfaces in the as-deposited unannealed sample, reacted completely during the brief anneal to form amorphous TiSi layers alternating with unreacted amorphous silicon layers.

The behavior of a non-reactive system is illustrated by Co-Si and Mo-Si multilayers. During anneals of these materials under conditions that cause significant changes in reactive systems (250° C for 1 s) there is no planar growth of the as-deposited intermixed region for the non-reactive systems. Only at longer, higher temperature anneals (300° C for 10 s) does a reaction take place, and it is the crystallization of the intermixed region instead of its growth as an amorphous layer.

Determination of which systems are reactive and which non-reactive has been based only on empirical studies. Attempts to classify systems with kinetic models [135] have proven inadequate [70]. Thus, in order to determine which of the spin-glass systems are reactive or non-reactive would require both annealing and calorimetric studies.

### 4.3 Effect of Interface Structure on Spin-Glass Properties

Planar growth of an amorphous silicide phase could explain the wide symmetrical intermixed layers seen in the 7 nm/ 7 nm Cu<sub>.85</sub>Mn<sub>.15</sub>/Si multilayer and possibly the complete amorphization of the 3 nm/ 7 nm Cu<sub>.85</sub>Mn<sub>.15</sub>/Si multilayers. The question that remains, however, is whether these interface structures existed during the measurements conducted for the spin-glass studies or if they resulted from the preparation of the TEM specimen. The fact that the LAXS data indicated that all the spin-glasses had some crystal-linity before the TEM sample preparation lends support to the idea of some alteration by sample preparation. The existence of as-deposited intermixed layers is supported, however, from the study of the spin-glasses themselves. Hoines et al. [18] found for the three systems observed in this study (AuFe/Si, CuMn/Si, and AgMn/Si) that it was necessary to decrease the thickness of the pure spin-glass layer from its intended fabrication value to account for the depression of the T<sub>g</sub> vs. spin-glass layer thickness curves from the expected trend (Figures 4.1 and 4.2)

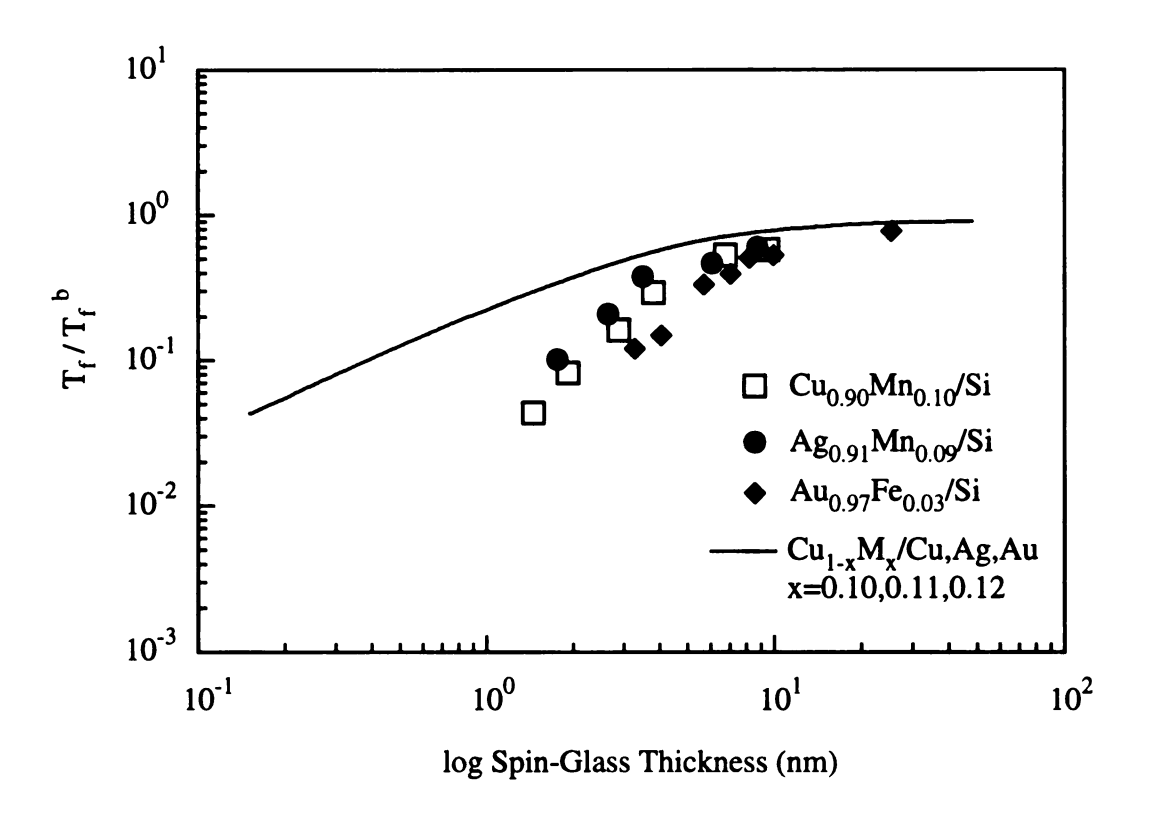


Figure 4.1 Finite-size effects of CuMn, AgMn, and AuFe spin-glasses with silicon interlayers. After Hoines [18].

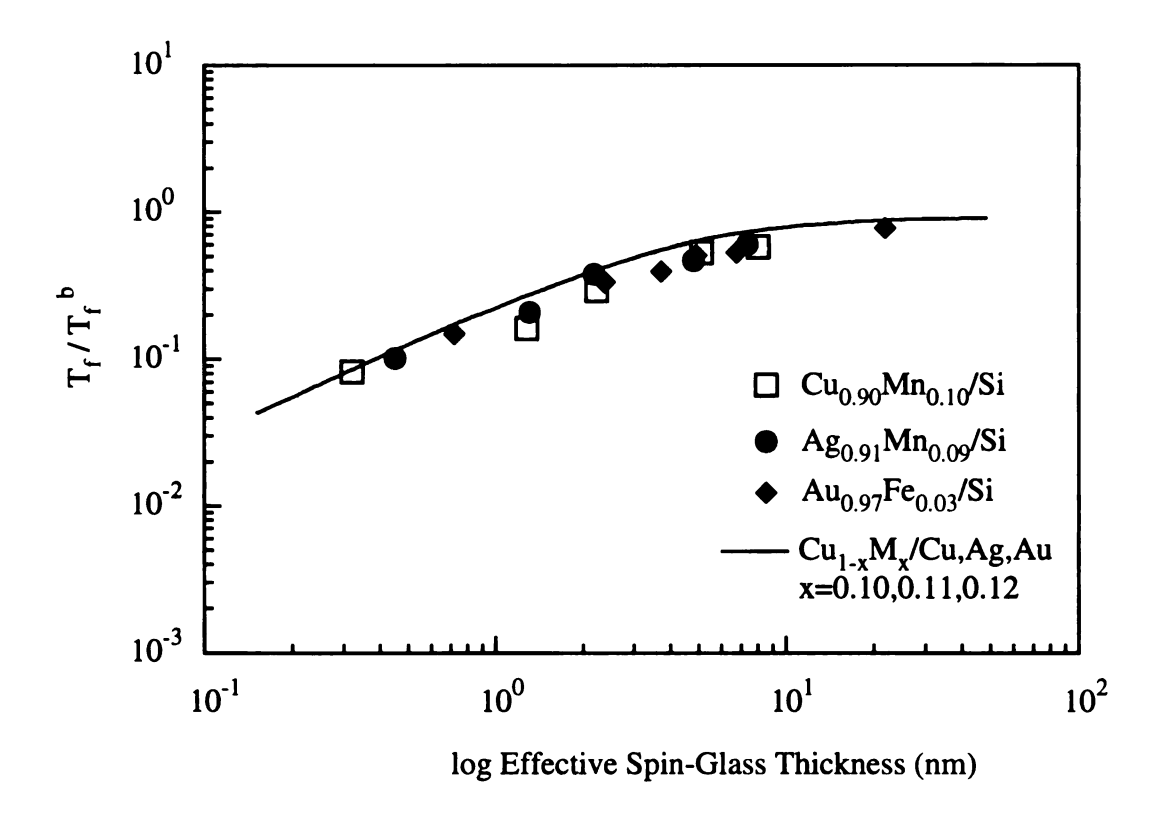
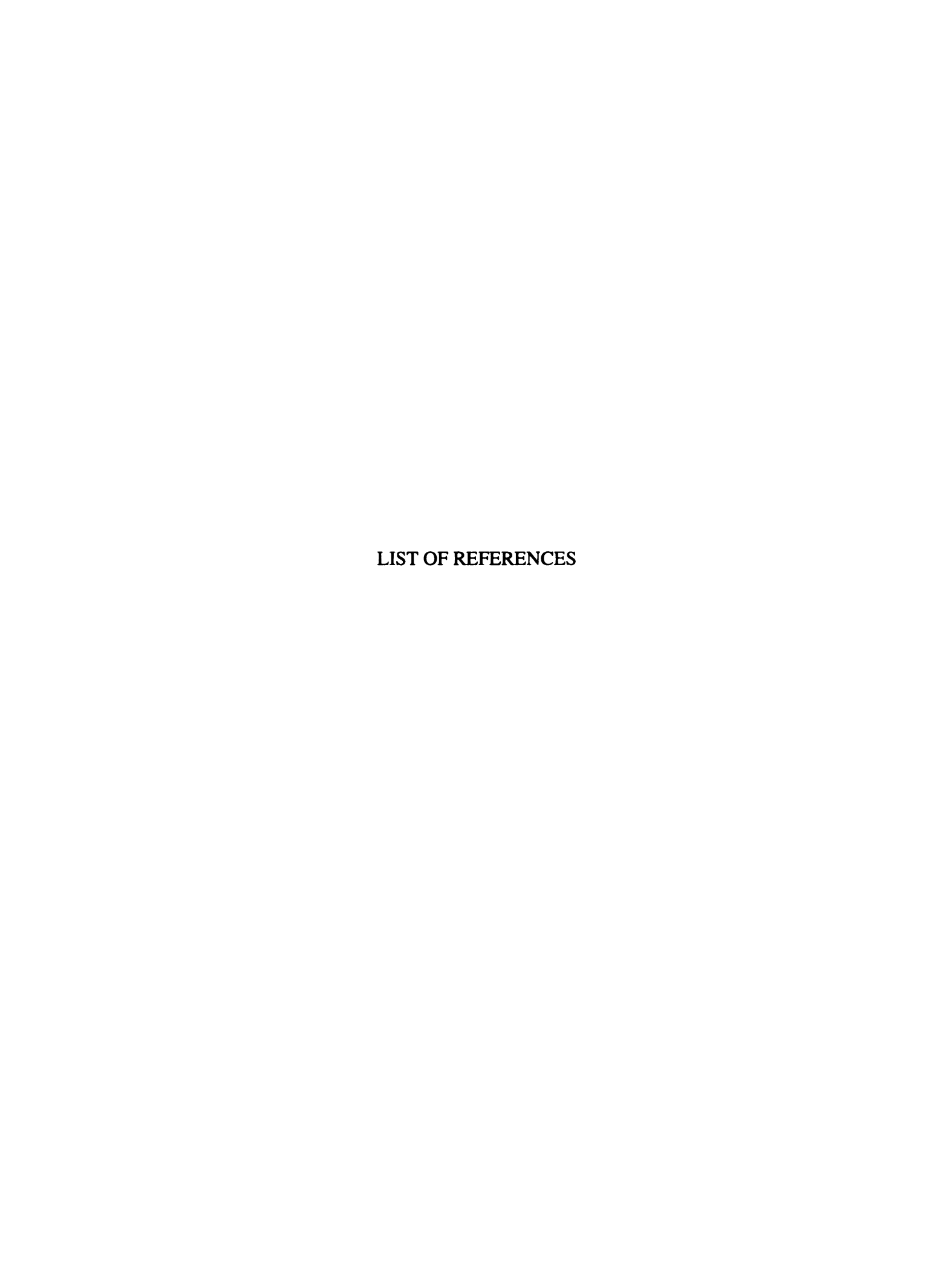


Figure 4.2 Finite-size effects of CuMn, AgMn, and AuFe spin-glasses with silicon interlayers and corrected spin-glass thicknesses. After Hoines [18].

#### CHAPTER 5 CONCLUSIONS

- Discrepancies in the results of the different methods used to characterize the spin-glass multilayers (LAXS, SAXS, CTEM, and HRTEM) indicate that sample preparation artifacts may be responsible for some of the observed interfacial structures.
- The varied interfacial regions observed in the HRTEM images of multilayers with the same composition but different layer thicknesses may also be due to variations in processing parameters (substrate temperature, sputtering rate) or sample geometry (spinglass layer thickness).
- Variations in the amount of interfacial mixing between systems of different compositions and the presence of asymmetrical or symmetrical interfacial regions on the top and bottom of the metal layer in metal/silicon multilayers indicate that a model more sophisticated than one based on the simple consideration of the relative penetration depths during sputtering of light versus heavy atoms is needed.
- Further modifications to the ion-milling procedures such as very-low angle (< 5°) and sector-control milling would minimize the amount of ion-milling needed, thereby allowing a systematic study of variations in fabrication parameters and their correlation to spin-glass properties to be undertaken with the effect of sample preparation artifacts minimized.



#### LIST OF REFERENCES

- [1] T. Shinjo (1987) Overview of Metallic Superlattice Studies, in Metallic Superlattices Artificially Structured Materials, eds. T. Shinjo and T. Takada, v. 49, Studies in Physical and Theoretical Chemistry, Elsevier Science Publishers B.V., Amsterdam, The Netherlands.
- [2] D.G. Stearns, R.S. Rosen, and S.P. Vernon (1991) High-Performance Multilayers for Soft X-Ray Projection Lithography, SPIE, 1547, 2-13.
- [3] J.M. Slaughter and C.M. Falco (1992) Advances in Multilayer X-Ray Optics, Nuc. Instr. Meth. Phys. Res., A319, 163-169.
- [4] M.B. Stearns (1982) Magnetization and Structure of Mn-Ni and Mn-Co Layered Magnetic Thin Films, J. Appl. Phys., 53(3), 2436-2438.
- [5] M.B. Stearns, C.H. Lee, and T.L. Groy (1989) Structural Studies of Co/Cr Multilayered Thin Films, Phys. Rev. B, 40(12), 8256-8269.
- [6] I.K. Schuller, J. Guimpel, and Y. Bruynseraede (1990) Artificially Layered Superconductors, MRS Bulletin, 15(7), 29-36.
- [7] V. Matijasevic and M.R. Beasley (1987) Superconductivity in Superlattices, in Metallic Superlattices Artificially Structured Materials, eds. T. Shinjo and T. Takada, v. 49, Studies in Physical and Theoretical Chemistry, Elsevier Science Publishers B.V., Amsterdam, The Netherlands.
- [8] G.G. Kenning, J.M. Slaughter, and J.A. Cowen (1987) Finite-Size Effects in a CuMn Spin-Glass, Phys. Rev. Lett., 59(22), 2596-2599.

- [9] G.G. Kenning (1988) Finite-Size Effects in Copper Manganese Spin-Glasses, Doctoral Dissertation, Michigan State University, E. Lansing, MI
- [10] J.A. Cowen, G.G. Kenning, and J. Bass (1988) Finite-Size Effects in a Metallic Spin-Glass (invited), J. Appl. Phys., 64(10), 5781-5784.
- [11] J.A. Cowen, G.G. Kenning, and J.M. Slaughter (1987) Magnetic Susceptibility and Magnetic Resonance of a Composition-Modulated Spin-Glass, J. Appl. Phys., 61(8), 4080-4082.
- [12] D.S. Fisher and D.A. Huse (1987) Static and Dynamic Behavior of Spin-Glass Films, Phys. Rev. B., 36(16), 8937-8940.
- [13] J. Vranken, C. Van Haessendonck, H. Vloeberghs, and Y. Bruynseraede (1989) Dimensional Cross-Over in Thin Film Spin-Glasses, Physica Scripta., T25, 348-352.
- [14] G.G. Kenning, J. Bass, W.P. Pratt Jr., D. Leslie-Pelecky, L. Hoines, W. Leach, M.L. Wilson, R. Stubi, and J.A. Cowen (1990) Finite-Size Effects in Cu-Mn Spin Glasses, Phys. Rev. B, 42(4), 2393-2415.
- [15] L. Sandlund, P. Grandberg, L. Lundgren, P. Norblad, P. Svedlindh, J.A. Cowen and G.G. Kenning (1990) Dynamics of Cu-Mn Spin-Glass Films, Phys. Rev. B, 40(1), 5252-5254.
- [16] P. Grandberg, P. Norblad, P. Svedlindh, L. Lundgren, R. Stubi, G.G. Kenning, D.L. Leslie-Pelecky, J. Bass, and J. Cowen (1990) Dimensionality Crossover in CuMn Spin-Glass Films, J. Appl. Phys., 67(9), 5252-5254.
- [17] J. Bass and J. Cowen (1992) Finite-Size Effects in Metallic Spin Glasses, in Recent Progress in Random Magnets, ed. D.H. Ryan, p. 177-206, World Scientific Publishing Co., Singapore.
- [18] L.M. Hoines (1994) Finite Size Effects and Coupling in Metallic Spin Glasses, Doctoral Dissertation, Michigan State University, E. Lansing, MI.

- [19] D.H. Ryan (1992) Exchange Frustration and Transverse Spin Freezing, in Recent Progress in Random Magnets, ed. D.H. Ryan, p. 1-40, World Scientific Publishing Co., Singapore.
- [20] T.W. Barbee (1990) Multilayer Optics of the Soft X-Ray and Extreme Ultraviolet, MRS Bulletin, 15(7), 37-44.
- [21] S.R. Herd, P. Chaudahri, and M.H. Brodsky (1972) Metal Contact Induced Crystallization in Films of Amorphous Silicon and Germanium, J. Non-Crystalline Solids, 7, 309-327.
- [22] A.S. Bhansali, D.H. Ko, and R. Sinclair (1990) Phase Reactions at Semiconductor Metallization Interfaces, J. of Electronic Materials, 19(11), 1171-1175.
- [23] R. Sinclair (1990) Study of Interfacial Reactions in Metal-Silicon and Related Systems by High-Resolution Electron Microscopy and Thermodynamic Analysis, Materials Transactions, JIM, 31(7), 628-635.
- [24] A.S. Bhansali, R. Sinclair, and A.E. Morgan (1990) A Thermodynamic Approach for interpreting Metallization Stability and Thin-Film Reactions Involving four Elements: Application to Integrated Circuit Contact Metallurgy, J. Appl. Phys., 68(3), 1043-1049.
- [25] I.K. Schuller, E.E. Fullerton, H. Vanderstraeten, and Y. Bruynseraede (1991) Quantitative X-Ray Diffraction of Superlattices and Interfaces, Mat. Res. Soc. Symp. Proc., 229, 41-52.
- [26] E.E. Fullerton, I.K. Schuller, and Y. Bruynseraede (1992) Quantitative X-Ray Diffraction from Superlattices, MRS Bulletin, 17(12), 33-38.
- [27] D.G. Stearns (1992) X-ray Scattering from Interfacial Roughness in Multilayer Structures, J. Appl. Phys., 71(9), 4286-4298.
- [28] E.E. Fullerton, I.K. Schuller, H. Vanderstraeten, and Y. Bruynseraede (1992) Structural Refinement of Superlattices from X-Ray Diffraction, Phys. Rev. B, 54(16), 1992.

- [29] B.M. Clemens and R. Sinclair (1990) Metastable Phase Formation in Thin Films and Multilayers, MRS Bulletin, 15(2), 19-28.
- [30] A.L. Greer (1986) Atomic Diffusion and Phase Transformation in Artificially layered Thin Films, Scripta Met., 20, 457-464.
- [31] A.L. Greer (1993) Diffusion and Phase Nucleation in Metallic Multilayers, J. Mag. Magn. Mater., 126, 89-95.
- [32] B.M. Clemens (1987) Effect of Sputtering Pressure on the Structure and Solid-State Reaction of Titanium-Nickel Compositionally Modulated Film, J. Appl. Phys., 61(9), 4525-4529.
- [33] R.B. Schwarz and W.L. Johnson (1983) Formation of an Amorphous Alloy by Solid-State Reaction of the Pure Polycrystalline Metals, Phys. Rev. Lett., 51(5), 415-418.
- [34] A.L. Greer (1990) Transformations of Metastable Phases, Phil. Mag., B61(4), 525-538.
- [35] B.M. Clemens (1984) Amorphous Zirconium-Nickel Films Formed by Solid State Reactions, J. Non-Cryst. Solids, 61&62, 817-822.
- [36] S.J. Pennycook (1989) Z-Contrast STEM for Materials Science, Ultramicroscopy, 30, 58-69.
- [37] D.G. Stearns, N.M. Ceglio, A.M. Hwaryluk, M.B. Stearns, A.K. Petford-Long, C.-H. Chang, K. Danzmann, M. Kuhne, P. Muller, and B. Wende (1986) TEM and X-Ray Analysis of Multilayer Mirrors and Beamsplitters, SPIE, 688, 91-98.
- [38] M.B. Stearns, A.K. Petford-Long, C.-H. Chang, D.G. Stearns, N.M. Ceglio, and A.M. Hawryluk (1987) X-ray-Optical Multilayer Structures Studied Using High Resolution Electron Microscopy, Mat. Res. Soc. Symp. Proc., 77, 345-350.

- [39] A.K. Petford-Long, M.B. Stearns, C.-H. Chang, S.R. Nutt, D.G. Stearns, N.M. Ceglio, and A.M. Hawryluk (1987) High-Resolution Electron Microscopy Study of X-ray Multilayer Structures, J. Appl. Phys., 61(4), 1422-1428.
- [40] S. Ogura, M. Niibe, Y. Watanabe, M. Hyayshida, and T. Iizuka (1988) Comparison of Soft X-ray mirrors fabricated by Electron Beam, DC-, RF-magnetron Sputtering and Ion Beam Sputtering Deposition, SPIE, 984, 140-148.
- [41] S. Ogura, M. Hyayshida, A. Ishizki, Y. Kato, and J.L. Wood (1988) Evaluation of Alternative Mo-Si Multilayer for Soft X-ray Mirrors by Electron Microscopy and X-Ray Diffraction, SPIE, 984, 140-148.
- [42] K. Holloway, K.B. Do, and R. Sinclair (1988) In-Situ and High-Resolution TEM Observations of Interfacial Reactions in Metal-Silicon Multilayers, Mat. Res. Soc. Symp. Proc., 103, 167-172.
- [43] R. Sinclair, K. Holloway, K.B. Kim, D.H. Ko, A.S. Bhansali, A.F. Schwartzman, and S. Ogawa (1989) Reaction and Structure at Metal-Semiconductor Interfaces, Inst. of Phys. Conf. Ser., 100(8), 599-607.
- [44] K. Holloway, K.B. Do, and R. Sinclair (1989) Interfacial Reactions on Annealing Molybdenum-Silicon Multilayers, J. Appl. Phys., 65(2), 474-480.
- [45] K. Holloway, R.Sinclair, and M.Nathan (1989) Amorphous Silicide Formation by Thermal Reaction: A Comparison of Several Metal-Silicon Systems, J. Vac. Sci. Tech., A7(3), 1479-1483.
- [46] M. Sudoh, R. Yokoyama, and M. Sumiya (1990) Soft X-ray Multilayers Fabricated by Electron-Beam Deposition, SPIE, 1343, 14-24.
- [47] J.M. Slaughter, P.A. Kearney, D.W. Schulze, C.H. Falco, C.R. Hills, E.B. Saloman, and R.N. Watts (1990) Interfaces in Mo/Si Multilayers, SPIE, 1343, 73-82.
- [48] M. Niibe, M. Hayashida, T. Iizuka, A. Miyake, Y. Watanabe, R. Takahashi, and Y. Fukuda (1990) Suppression of Columnar-Structure Formation in Mo-Si Layered Synthetic Microstructures, SPIE, 1343, 2-13.

- [49] D.L. Windt, R. Hull, and W.K. Waskiewicz (1990) Interface Characterization of XUV Multilayer Reflectors Using HRTEM and X-Ray and XUV Reflectance, SPIE, 1343, 292-308.
- [50] H. Takenaka, Y. Ishii, H. Kinoshita, and K. Kurihara (1990) Soft and Hard X-ray Reflectivities of Multilayers Fabricated by Alternating-Material Sputter Deposition, SPIE, 1345, 213-224.
- [51] J.M. Slaughter, A. Shapiro, P.A. Kearney, and C.M. Falco (1991) Growth of Molybdenum on Silicon: Structure and Interface Formation, Phys. Rev. B., 44(8), 3854-3863.
- [52] R.S. Rosen, M.A. Viliardos, M.E. Kassner, D.G. Stearns, and S.P. Vernon (1991) Thermal Stability of Mo/Si Multilayers, SPIE, 1547, 212-220.
- [53] P. Boher, P. Houdy, L. Hennet, M. Kuhne, P. Muller, J.P. Forntier, P. Trouslard, C. Senillou, J.C. Joud, and P. Ruterana (1991) Structural Characteristics and Performance of RF-Sputtered Mo/Si and Co/Si Multilayers for Soft X-Ray Optics, SPIE, 1574, 21-38.
- [54] D.G. Stearns, R.S. Rosen, and S.P. Vernon (1991) Fabrication of High-Reflectance Mo-Si Multilayer Mirrors by Planar-Magnetron Sputtering, J. Vac. Sci. Tech., A9(5), 2662-2669.
- [55] D.L. Windt, R. Hull, and W.K. Waskiewicz (1992) Interface Imperfections in Metal/Si Multilayers, J. Appl. Phys., 71(6), 2675-2678.
- [56] Y. Cheng, D.J. Smith, M.B. Stearns, and D.G. Stearns (1992) Imaging X-Ray Multilayer Structures Using Cross-Sectional High Resolution Electron Microscopy, J. Appl. Phys., 72(11), 5165-5171.
- [57] J. Liu, Y. Cheng, J.M. Cowley, and M.B. Stearns (1992) High-Angle Annular Dark-Field Microscopy of Mo/Si Multilayer Structures, Ultramicroscopy, 40, 352-364.
- [58] M.B. Stearns, C.-H. Chang, and D.G. Stearns (1992) Optimization of Growth Conditions of Vapor Deposited Mo/Si Multilayers, J. Appl. Phys., 71(1), 187-195.

- [59] A.F. Jankowski (1992) On Eliminating Deposition-Induced Amorphization of Interfaces in Refractory Metal Multilayer Systems, Thin Solid Films, 220, 166-171.
- [60] R.S. Rosen, D.G. Stearns, M.E. Kassner, J.-I. Koike, Y. Cheng, and S.P. Vernon (1993) Kinetics of Interlayer Growth and Changes in Residual Elastic Strain During Annealing of Mo/Si Multilayers, Nanostructured Materials, 3, 195-202.
- [61] R.S. Rosen, D.G. Stearns, M.A. Viliardos, M.E. Kassner, S.P. Vernon, and Y. Cheng (1993) Silicide Layer Growth Rates in Mo/Si Multilayers, Applied Optics, 32(34), 6975-6980.
- [62] S.P. Vernon, D.G. Stearns, and R.S. Rosen (1993) Ion-Assisted Sputter Deposition of Molybdenum-Silicon Multilayers, Applied Optics, 32(34), 6969-6974.
- [63] D.G. Stearns, R.S. Rosen, and S.P. Vernon (1993) Multilayer Mirror Technology for Soft-X-Ray Projection Lithography, Applied Optics, 32(34), 6952-6960.
- [64] J.K. Weiss, W.J. de Ruijeter, M. Gajdardziska-Josifovska, M.R. McCartney, and D.J. Smith (1993) Applications of Electron Holography to the Study of Interfaces, Ultramicroscopy, 50, 301-311.
- [65] H. Azuma, A. Takeichi, I. Konomi, Y. Watanabe, and S. Noda (1993) Thermally Induced Structural Modification of Nanometer-Order Mo/Si Multilayers by the Spectral Reflectance of Laser-Plasma Soft X-Rays, Jpn. J. Appl. Phys., 32(5A), 2078-2082.
- [66] A. Konkol, A. Sulyok, M. Menyhard, and A. Barna (1994) Auger In-Depth Profiling of Mo-Si Multilayers, J. Vac. Sci. Tech., A12(2), 436-442.
- [67] R. Schlatmann, C. Lu, J. Verhoeven, E.J. Puik, and M.J. van der Wiel (1994) Modification by Ar and Kr Ion Bombardment of Mo/Si X-ray Multilayers, Applied Surface Science, 78, 147-157.
- [68] K. Holloway and R. Sinclair (1987) Interfacial Reactions in Titanium-Silicon Multilayers, Mat. Res. Soc. Symp. Proc., 77, 357-362.

- [69] K. Holloway and R. Sinclair (1987) Amorphous Ti-Si alloy formed by interdiffusion of amorphous Si and Crystalline Ti Multilayers, J. Appl. Phys., 61(4), 1359-1364.
- [70] M. Nathan (1988) Solid Phase Reactions in Free-Standing Layered M-Si (M=Ti, V, Cr, Co) Films, J. Appl. Phys., 63(11), 5534-5540.
- [71] I.J.M.M. Raaijmakers, A.H. Reader, and P.H. Oosting (1988) The Formation of An Amorphous Silicide by Thermal Reaction of Sputter-Deposited Ti and Si Layers, J. Appl. Phys., 63(8), 2790-2795.
- [72] W. Lur and L.J. Chen (1989) Interfacial Reactions of Titanium Thin Films on BF<sup>+2</sup>-implanted (001)Si, J. Appl. Phys., 66(8), 3604-3611.
- [73] K. Holloway, P. Moine, J. Delage, and R. Sinclair (1991) Structure of An Amorphous Ti-Si alloy Formed by Thermal Reaction, J. Non-Cryst. Solids, 334, 133-140.
- [74] E. Ma, L.A. Clevenger, C.V. Thompson, and K.N. Tu (1990) Kinetic and Thermodynamic Aspects of Phase Evolution in Ti/a-Si Multilayer Films, Mat. Res. Soc. Symp. Proc., 187, 83-88.
- [75] I.J.M.M. Raaijmakers and K.B. Kim (1990) A Comparison of the Reaction of Titanium with Amorphous and Monocrystalline Silicon, J. Appl. Phys., 67(10), 6255-6264.
- [76] S.-I. Ogawa, T. Kouzaki, T. Yoshida, and R. Sinclair (1991) Interface Microstructure of Titanium Thin-Film/Silicon Single-Crystal Substrate Correlated with Electrical Barrier Heights, J. Appl. Phys., 70(2), 827-832.
- [77] T.P. Nolan, R. Sinclair, and R. Beyers (1992) Modeling of Agglomeration in Polycrystalline Films: Application to TiSi<sub>2</sub> on a Silicon Substrate, J. Appl. Phys., 71(2), 720-724.
- [78] R. Sinclair and T.J. Konno (1993) Annealing of Metal-Metalloid Multilayers Studied by In-Situ Electron Microscopy, J. Mag. Magn. Mater., 126, 108-112.

- [79] S.R. Nutt and J.E. Keem (1988) Atomic Level Investigations of W/Si Multilayers by High Resolution TEM and X-Ray Scattering, Mat. Res. Soc. Symp. Proc., 103, 87-94.
- [80] V. Dupuis, M.F. Ravet, C. Tete, M. Piecuch, and B. Vidal (1990) Characteristics and Thermal Behavior of W/Si Multilayers With Well-Defined Interfaces, J. Appl. Phys., 68(7), 3348-3355.
- [81] B.A. Vidal and J.C. Marfaing (1989) X-Ray Reflectivity and Transmission Electron Microscopy Studies on Thin and Ultrathin W/C and W/Si Multilayers Structures, J. Appl. Phys., 65(9), 3453-3458.
- [82] W.C. Shih and W.M. Stobbs (1990) The Measurement of the Roughness of W/Si Multilayers Using The Fresnel Method, Ultramicroscopy, 32, 219-239.
- [83] M. Brunel, S. Enzo, M. Jergel, S. Luby, E. Majkova, and I. Vavra (1993) Structural Characterization and Thermal Stability of W/Si multilayers, J. Mater. Res., 8(10), 2600-2607.
- [84] L.A. Clevenger, C.V. Thompson, R.R. de Avillez, and K.N. Tu (1989) Kinetics and Thermodynamics of Amorphous Silicide Formation in Nickel/Amorphous-Silicon Multilayer Thin Films, Mat. Res. Soc. Symp. Proc., 148, 77-82.
- [85] C.V. Thompson, L.A. Clevenger, R.R. de Avillez, and H. Miura (1990) Kinetics and Thermodynamics of Amorphous Silicide Formation in Nickel/Amorphous-Silicon Multilayer Thin Films, Mat. Res. Soc. Symp. Proc., 187, 61-70.
- [86] K. Holloway and L. Clevenger (1990) Microstructural Aspects of Nickel Silicide Formation in Evaporated Nickel-Silicon Multilayer Thin Films, Mat. Res. Soc. Symp. Proc., 159, 153-157.
- [87] W.H. Wang, H.Y. Bai, Y. Zhang, H. Chen, and W.K. Wang (1993) Solid-State Amorphization Reaction in Polycrystalline and Amorphous Si Multilayer, J. Appl. Phys., 73(11), 7217-7221.
- [88] W.H. Wang, H.Y. Bai, Y. Zhang, and W.K. Wang (1993) Phase Selection in Interfacial Reaction of Ni/Amorphous Si Multilayers, J. Appl. Phys., 73(9), 4313-4318.

- [89] W.H. Wang, H.Y. Bai, Y. Zhang, H. Chen, and W.K. Wang (1993) Measurements of interdiffusion in Compositionally Modulated Amorphous Ni/Si Multilayers by In-Situ X-Ray Diffraction, Mat. Sci. and Eng., B(22), 211-216.
- [90] W.H. Wang and W.K. Wang (1994) Amorphization Phenomenon in Ni/Amorphous Si Multilayers, J. Mater. Res., 9(2), 401-405.
- [91] M.B. Stearns, C.H. Lee, C.-H. Chang, and A.K. Petford-Long (1988) Magnetic, X-ray, and TEM Studies of Several Multilayer Systems, in Metallic Multilayers and Epitaxy, eds. M.Hong, S. Wolf, and D.C. Gibser, p. 55-75, The Metallurgical Society, Warrendale, PA.
- [92] H. Miura, E.N. Ma, and C.V. Thompson (1992) Initial Evolution of Cobalt Silicides in the Cobalt/Amorphous-Silicon Thin Film System, Mat. Res. Soc. Symp. Proc., 230, 139-144.
- [93] T.J. Konno and R. Sinclair (1992) Crystallization of Silicon in Aluminum/Amorphous-Silicon Multilayers, Phil. Mag. B, 66(6), 749-765.
- [94] T.J. Konno and R. Sinclair (1992) Crystallization of Amorphous Silicon in Al/Si Multilayers, Mat. Res. Soc. Symp. Proc., 230, 189-194.
- [95] T. Nakayama, T.J. Konno, H. Satoh, and R. Sinclair (1993) Structure and Corrosion Properties of Al/Si Multilayers, J. Mag. Magn. Mater., 126, 167-169.
- [96] E.E. Fullerton, J. Pearson, C.H. Sowers, S.D. Bader, X.Z. Wu, and S.K. Sinha (1993) Interfacial Roughness of Sputtered Multilayers: Nb/Si, Phys. Rev. B., 48(23), 17432-17444.
- [97] Y. Cheng, J. Liu, M.B. Stearns, and D.G. Stearns (1991) Annealing Studies of Ru/Si Multilayer by High-Angle Annular Dark Field Microscopy and HREM, SPIE, 1547, 167-175.
- [98] D.G. Stearns, R.S. Rosen, and S.P. Vernon (1991) High-Performance Multilayers for Soft X-Ray Projection Lithography, SPIE, 1547, 2-13.

- [99] Z.G. Li, D.J. Smith, S.-C. Y. Tsen, P. Boher, and P. Houdy (1991) Investigations of Soft X-Ray Applications by High-Resolution Electron Microscopy, J. Appl. Phys., 70(6), 2905-2910.
- [100] Y. Cheng, J. Liu, M.B. Stearns, and D.G. Stearns (1992) Characterization of Rh/Si Multilayer Structure by HREM and HAADF, Proc. 50th Ann. Meet. of EMSA., eds: G.W. Bailey, J. Bentley, and J.A. Small, San Francisco Press, San Francisco, CA, 122-123.
- [101] L.A. Clevenger, C.V. Thompson, R.R. de Avillez, and E. Ma (1990) Nucleation Controlled Phase Selection in Vanadium/Amorphous-Silicon Multilayer Thin Films, J. Vac. Sci. Tech., A8(3), 1566-1571.
- [102] L.S. Xiu, B. Wang, W.H. Liu, S.L. Ying, X.P. Wang, and Z.Q. Wu (1992) Structural Study of Sputtered Pd/Si Multilayers, 83(3), 1-3.
- [103] T.L. Lee and L.J. Chen (1993) Interfacial Reactions in Ultrahigh Vacuum Deposited Y/Si Multilayer Thin Films, J. Appl. Phys., 75(4), 2007-2014.
- [104] B.L. Evans, J. Al-Dabbagh, and B.J. Kent (1988) The Soft X-Ray to EUV Performance of Plane and Concave Pt-Si Multilayer Mirrors, SPIE, 984, 104-110.
- [105] C. Dufour, A. Bruson, G. Marchal, B. George, and P. Mangin (1991) Structural and Magnetic Profiles in Fe/Si Multilayers, J. Mag. Magn. Mater., 93, 545-551.
- [106] R.E. Somekh (1984) The Thermalization of Energetic Atoms During the Sputtering Process, J. Vac. Sci. Tech., A2(3), 1285-1291.
- [107] D.A. Howell, J.W. Heckman Jr., and M.A. Crimp (1995) Preparation of Metal Multilayer Cross-Sections Using Ultramicrotomy, J. Microscopy, accepted for publication.
- [108] A.R. Spurr (1969) A Low-Viscosity Epoxy Resin Embedding Medium for Electron Microscopy, Ultrastructure Research, 26, 31-43.

- [109] R.S. Timsit, J.L. Hutchison, and M.C. Thornton (1984) Preparation of Metal Specimens for HREM by Ultramicrotomy, Ultramicroscopy, 15, 371-374.
- [110] A.F. Marshall and D.C. Dobbertin (1986) Cross-Sectioning of Layered Thin Films by Ultramicrotomy, Ultramicroscopy, 19, 69-73.
- [111] T. Malis (1988) AEM Specimen Preparation Something Old and Something New, EMAG '87 Analytical Electron Microscopy Workshop Proc., ed. G. W. Lorimer, p. 127-134, Institute of Metals, London.
- [112] T.F. Malis and D. Steele (1990) Ultramicrotomy for Materials Science, Mat. Res. Soc. Symp. Proc., 199, 3-42.
- [113] J.P. Heuer and D.G. Howitt (1990) A Novel Technique for the Preparation of Thin Films for Cross-Sectional Transmission Electron Microscopy, J. Electron Microscopy, Tech., 14, 79-82.
- [114] T. Malis and D. Steele (1992) Thickness Variations and Surface Layers in Ultramicrotomed Sections and Their Effects on Elemental Mapping, Mat. Res. Soc. Symp. Proc., 254, 257-270.
- [115] C.E. Lyman, R. Anderson, and T. Malis (1993) Thin-Specimen Preparation for Heterophase Interfaces, Proc. 51st Annual Meeting MSA, eds. G.W. Bailey and C.L. Rieder, 838-839, San Francisco Press, San Francisco, CA.
- [116] J.C. Bravman and R. Sinclair (1984) The Preparation of Cross-Section Specimens for Transmission Electron Microscopy, J. of Electron Micro. Tech., 1, 53-61.
- [117] S.B. Newcomb, C.B. Boothroyd, and W.M. Stobbs (1985) Specimen Preparation Methods for the Examination of Surfaces and Interfaces in the Transmission Electron Microscope, J. Microscopy, 140(2), 195-207.
- [118] K. Barmak, D.A. Rudman, and S. Foner (1990) The Preparation of Cross-Sectional Transmission Electron Microscopy Specimens of Nb/Al Multilayer Thin Films on Sapphire Substrates, J. Elect. Micro. Tech., 249-253.

- [119] T.D. Nguyen, R. Gronsky, and J.B. Kortright (1991) Cross-Sectional Transmission Electron Microscopy of X-ray Multilayer Thin-Film Structures, J. Elect. Micro. Tech., 19, 473-485.
- [120] C. Wan and M. Dupeux (1992) Preparation of Cross-Section Specimens for Transmission Electron Microscopy From α-Al<sub>2</sub>O<sub>3</sub>/Ni Solid State Bonded Bicrystal Interfaces, Micro. Res. Tech., 23, 248-251.
- [121] U. Helmersson and J.-E. Sundgren (1986) Cross-Section Preparation for TEM Film-Substrate Combinations With a Large Difference in Sputtering Yields, J. Elect. Micro. Tech., 4, 361-369.
- [122] H.L. Humiston, B.M. Tracy, M. Lawrence, and A. Dass (1992) Preparation of Large Thin Area VLSI TEM Specimens By Dimpling with a "Flattening Tool", Mat. Res. Soc. Symp. Proc., 254, 211-221.
- [123] M.C. Madden and P. Crafard (1989) A Variation of Transmission Electron Microscope Sample Preparation for VLSI Analysis, J. Elect. Micro. Tech., 11, 161-166.
- [124] E.M. Zielinski and B. Tracy (1992) Comparative Study of Ion Milling Techniques in Cross-Sectional Transmission Electron Microscope Specimen Preparation, Micro. Res. Tech., 22, 199-206.
- [125] F. Shaapur and K.A. Watson (1992) Minimization of Non-Uniform Ion-Thinning in Thin Film Transverse Specimens for Transmission Electron Microscopy, Mat. Res. Soc. Symp., 254, 153-158.
- [126] D. Bahnck and R. Hull (1990) Experimental Measurement of Transmission Electron Microscope Specimen Temperature During Ion Milling, Mat. Res. Soc. Symp., 199, 253-261.
- [127] D.G. Howitt (1984) Ion-Milling of Materials Science Specimens for Electron Microscopy: A Review, J. Elect. Micro. Tech., 1, 405-414.
- [128] D.J. Barber (1993) Radiation Damage in Ion-Milled Specimens: Characteristics, Effects and Methods of Damage Limitation, Ultramicroscopy, 52, 101-125.

- [129] A. Romano, J. VanHellemont, H. Bender, and J.R. Morante (1989) A Fast Preparation Technique for High Quality Plan View and Cross-Section TEM Specimens of Semiconducting Materials, Ultramicroscopy, 31, 183-192.
- [130] A. Romano, J. VanHellemont, and H. Bender (1990) A Fast and Precise Specimen Preparation Technique for TEM Investigation of Prespecified Areas of Semiconductor Devices, Mat. Res. Soc. Symp. Proc., 199, 167-176.
- [131] F. Shaapur and M. Park (1990) A Streamlined Technique for Preparation of Transverse Specimens for Transmission Electron Microscopy, Mater. Res. Soc. Symp. Proc., 199, 177-180.
- [132] O. Scherzer (1949) The Theoretical Resolution Limit of the Electron Microscope, J. Appl. Phys., 20, 20-29.
- [133] P. Donovan, B. George, A. Bruson, C. Dufour, G. Marchal, and P. Mangin (1991) Interpretation of Transmission Electron Microscope Images of Amorphous Silicon/Germanium and Silicon/Iron Multilayers. J. Appl. Phys., 69(3), 1371-1376.
- [134] J.M. Cowley (1986) Diffraction Physics, 2nd ed., North-Holland, New York, 287.
- [135] R.W. Bene (1987) A Kinetic Model for Solid-State Silicide Nucleation, J. Appl. Phys., 61 (5), 1826-1833.

